



# The Dark Energy Survey: Data Release 1

T. M. C. Abbott<sup>1</sup>, F. B. Abdalla<sup>2,3</sup>, S. Allam<sup>4</sup>, A. Amara<sup>5</sup>, J. Annis<sup>4</sup> , J. Asorey<sup>6,7,8</sup>, S. Avila<sup>9,10</sup>, O. Ballester<sup>11</sup>, M. Banerji<sup>12,13</sup>, W. Barkhouse<sup>14</sup>, L. Baruah<sup>15</sup>, M. Baumer<sup>16,17,18</sup>, K. Bechtol<sup>19</sup>, M. R. Becker<sup>16,17</sup>, A. Benoit-Lévy<sup>2,20,21</sup>, G. M. Bernstein<sup>22</sup>, E. Bertin<sup>20,21</sup>, J. Blazek<sup>23,24</sup>, S. Bocquet<sup>25</sup> , D. Brooks<sup>2</sup> , D. Brout<sup>22</sup>, E. Buckley-Geer<sup>4</sup>, D. L. Burke<sup>17,18</sup> , V. Busti<sup>26,27</sup>, R. Campisano<sup>26</sup>, L. Cardiel-Sas<sup>11</sup>, A. Carnero Rosell<sup>26,28</sup>, M. Carrasco Kind<sup>29,30</sup> , J. Carretero<sup>11</sup>, F. J. Castander<sup>31,32</sup> , R. Cawthon<sup>33</sup>, C. Chang<sup>33</sup>, X. Chen<sup>34</sup>, C. Conselice<sup>35</sup> , G. Costa<sup>26</sup>, M. Crocce<sup>31,32</sup>, C. E. Cunha<sup>17</sup>, C. B. D'Andrea<sup>22</sup>, L. N. da Costa<sup>26,28</sup>, R. Das<sup>34</sup>, G. Daues<sup>29</sup>, T. M. Davis<sup>7,8</sup>, C. Davis<sup>17</sup>, J. De Vicente<sup>36</sup>, D. L. DePoy<sup>37</sup>, J. DeRose<sup>16,17</sup> , S. Desai<sup>38</sup>, H. T. Diehl<sup>4</sup>, J. P. Dietrich<sup>39,40</sup>, S. Dodelson<sup>41</sup>, P. Doel<sup>2</sup>, A. Drlica-Wagner<sup>4</sup> , T. F. Eifler<sup>42,43</sup>, A. E. Elliott<sup>44</sup>, A. E. Evrard<sup>34,45</sup>, A. Farahi<sup>34</sup>, A. Fausti Neto<sup>26</sup>, E. Fernandez<sup>11</sup>, D. A. Finley<sup>4</sup>, B. Flaugher<sup>4</sup>, R. J. Foley<sup>46</sup>, P. Fosalba<sup>31,32</sup>, D. N. Friedel<sup>29</sup>, J. Frieman<sup>4,33</sup>, J. García-Bellido<sup>10</sup> , E. Gaztanaga<sup>31,32</sup>, D. W. Gerdes<sup>34,45</sup> , T. Giannantonio<sup>12,13,47</sup>, M. S. S. Gill<sup>16,17,18</sup>, K. Glazebrook<sup>6</sup> , D. A. Goldstein<sup>48,49</sup> , M. Gower<sup>29</sup>, D. Gruen<sup>17,18</sup> , R. A. Gruendl<sup>29,30</sup> , J. Gschwend<sup>26,28</sup>, R. R. Gupta<sup>25,48</sup>, G. Gutierrez<sup>4</sup>, S. Hamilton<sup>34</sup> , W. G. Hartley<sup>2,5</sup>, S. R. Hinton<sup>7</sup>, J. M. Hislop<sup>15</sup>, D. Hollowood<sup>50</sup> , K. Honscheid<sup>23,44</sup>, B. Hoyle<sup>47,51</sup>, D. Huterer<sup>34</sup>, B. Jain<sup>22</sup>, D. J. James<sup>52</sup>, T. Jeltema<sup>50</sup>, M. W. G. Johnson<sup>29</sup>, M. D. Johnson<sup>29</sup>, T. Kacprzak<sup>5</sup>, S. Kent<sup>4,33</sup>, G. Khullar<sup>33</sup>, M. Klein<sup>40,51</sup>, A. Kovacs<sup>11</sup>, A. M. G. Koziol<sup>29</sup>, E. Krause<sup>42,43</sup>, A. Kremin<sup>34</sup>, R. Kron<sup>4,53</sup>, K. Kuehn<sup>54</sup> , S. Kuhlmann<sup>25</sup>, N. Kuropatkin<sup>4</sup>, O. Lahav<sup>2</sup>, J. Lasker<sup>33,53</sup>, T. S. Li<sup>4</sup>, R. T. Li<sup>29</sup>, A. R. Liddle<sup>55</sup>, M. Lima<sup>26,27</sup>, H. Lin<sup>4</sup>, P. López-Reyes<sup>36</sup>, N. MacCrann<sup>23,44</sup>, M. A. G. Maia<sup>26,28</sup>, J. D. Maloney<sup>29</sup>, M. Manera<sup>11,74</sup>, M. March<sup>22</sup>, J. Marriner<sup>4</sup>, J. L. Marshall<sup>37</sup>, P. Martini<sup>23,56</sup> , T. McClintock<sup>57</sup>, T. McKay<sup>34</sup>, R. G. McMahon<sup>12,13</sup> , P. Melchior<sup>58</sup> , F. Menanteau<sup>29,30</sup>, C. J. Miller<sup>34,45</sup>, R. Miquel<sup>11,59</sup> , J. J. Mohr<sup>39,40,51</sup>, E. Morganson<sup>29</sup> , J. Mould<sup>6</sup> , E. Neilsen<sup>4</sup>, R. C. Nichol<sup>9</sup>, F. Nogueira<sup>26</sup>, B. Nord<sup>4</sup> , P. Nugent<sup>48</sup> , L. Nunes<sup>26</sup>, R. L. C. Ogando<sup>26,28</sup>, L. Old<sup>35,60</sup>, A. B. Pace<sup>37</sup>, A. Palmese<sup>2</sup> , F. Paz-Chinchón<sup>29</sup>, H. V. Peiris<sup>2</sup>, W. J. Percival<sup>9</sup>, D. Petravick<sup>29</sup>, A. A. Plazas<sup>43</sup>, J. Poh<sup>33</sup>, C. Pond<sup>29</sup>, A. Porredon<sup>31,32</sup>, A. Pujol<sup>31,32</sup>, A. Refregier<sup>5</sup>, K. Reil<sup>18</sup>, P. M. Ricker<sup>29,30</sup> , R. P. Rollins<sup>61</sup>, A. K. Romer<sup>15</sup> , A. Roodman<sup>17,18</sup> , P. Rooney<sup>15</sup>, A. J. Ross<sup>23</sup>, E. S. Rykoff<sup>17,18</sup>, M. Sako<sup>22</sup>, M. L. Sanchez<sup>26</sup>, E. Sanchez<sup>36</sup>, B. Santiago<sup>26,62</sup>, A. Saro<sup>40,63</sup>, V. Scarpine<sup>4</sup>, D. Scolnic<sup>33</sup>, S. Serrano<sup>31,32</sup>, I. Sevilla-Noarbe<sup>36</sup>, E. Sheldon<sup>64</sup>, N. Shipp<sup>33</sup> , M. L. Silveira<sup>26</sup>, M. Smith<sup>65</sup> , R. C. Smith<sup>1</sup>, J. A. Smith<sup>66</sup>, M. Soares-Santos<sup>4,67</sup> , F. Sobreira<sup>26,68</sup> , J. Song<sup>69</sup>, A. Stebbins<sup>4</sup>, E. Suchyta<sup>70</sup>, M. Sullivan<sup>65</sup> , M. E. C. Swanson<sup>29</sup>, G. Tarle<sup>34</sup> , J. Thaler<sup>71</sup>, D. Thomas<sup>9</sup>, R. C. Thomas<sup>48</sup>, M. A. Troxel<sup>23,44</sup>, D. L. Tucker<sup>4</sup>, V. Vikram<sup>25</sup>, A. K. Vivas<sup>1</sup> , A. R. Walker<sup>1</sup> , R. H. Wechsler<sup>16,17,18</sup> , J. Weller<sup>39,47,51</sup>, W. Wester<sup>4</sup>, R. C. Wolf<sup>22</sup>, H. Wu<sup>44</sup>, B. Yanny<sup>4</sup> , A. Zenteno<sup>1</sup>, Y. Zhang<sup>4</sup>, J. Zuntz<sup>55</sup>  
(DES Collaboration),  
and  
S. Juneau<sup>72</sup> , M. Fitzpatrick<sup>72</sup>, R. Nikutta<sup>72</sup>, D. Nidever<sup>72,73</sup> , K. Olsen<sup>72</sup> , and A. Scott<sup>72</sup>  
(NOAO Data Lab)

<sup>1</sup> Cerro Tololo Inter-American Observatory, National Optical Astronomy Observatory, Casilla 603, La Serena, Chile<sup>2</sup> Department of Physics & Astronomy, University College London, Gower Street, London, WC1E 6BT, UK<sup>3</sup> Department of Physics and Electronics, Rhodes University, P.O. Box 94, Grahamstown, 6140, South Africa<sup>4</sup> Fermi National Accelerator Laboratory, P.O. Box 500, Batavia, IL 60510, USA<sup>5</sup> Department of Physics, ETH Zurich, Wolfgang-Pauli-Strasse 16, CH-8093 Zurich, Switzerland<sup>6</sup> Centre for Astrophysics & Supercomputing, Swinburne University of Technology, Victoria 3122, Australia<sup>7</sup> School of Mathematics and Physics, University of Queensland, Brisbane, QLD 4072, Australia<sup>8</sup> ARC Centre of Excellence for All-sky Astrophysics (CAASTRO)<sup>9</sup> Institute of Cosmology & Gravitation, University of Portsmouth, Portsmouth, PO1 3FX, UK<sup>10</sup> Instituto de Física Teórica UAM/CSIC, Universidad Autónoma de Madrid, E-28049 Madrid, Spain<sup>11</sup> Institut de Física d'Altes Energies (IFAE), The Barcelona Institute of Science and Technology, Campus UAB, E-08193 Bellaterra (Barcelona) Spain<sup>12</sup> Kavli Institute for Cosmology, University of Cambridge, Madingley Road, Cambridge CB3 0HA, UK<sup>13</sup> Institute of Astronomy, University of Cambridge, Madingley Road, Cambridge CB3 0HA, UK<sup>14</sup> University of North Dakota, Department of Physics and Astrophysics, Witmer Hall, Grand Forks, ND 58202, USA<sup>15</sup> Department of Physics and Astronomy, Pevensey Building, University of Sussex, Brighton, BN1 9QH, UK<sup>16</sup> Department of Physics, Stanford University, 382 Via Pueblo Mall, Stanford, CA 94305, USA<sup>17</sup> Kavli Institute for Particle Astrophysics & Cosmology, P.O. Box 2450, Stanford University, Stanford, CA 94305, USA<sup>18</sup> SLAC National Accelerator Laboratory, Menlo Park, CA 94025, USA<sup>19</sup> LSST, 933 North Cherry Avenue, Tucson, AZ 85721, USA; [kbechtol@lsst.org](mailto:kbechtol@lsst.org)<sup>20</sup> Sorbonne Universités, UPMC Univ Paris 06, UMR 7095, Institut d'Astrophysique de Paris, F-75014, Paris, France<sup>21</sup> CNRS, UMR 7095, Institut d'Astrophysique de Paris, F-75014, Paris, France<sup>22</sup> Department of Physics and Astronomy, University of Pennsylvania, Philadelphia, PA 19104, USA<sup>23</sup> Center for Cosmology and Astro-Particle Physics, The Ohio State University, Columbus, OH 43210, USA<sup>24</sup> Institute of Physics, Laboratory of Astrophysics, École Polytechnique Fédérale de Lausanne (EPFL), Observatoire de Sauverny, 1290 Versoix, Switzerland<sup>25</sup> Argonne National Laboratory, 9700 South Cass Avenue, Lemont, IL 60439, USA<sup>26</sup> Laboratório Interinstitucional de e-Astronomia—LINEA, Rua Gal. José Cristino 77, Rio de Janeiro, RJ—20921-400, Brazil<sup>27</sup> Departamento de Física Matemática, Instituto de Física, Universidade de São Paulo, CP 66318, São Paulo, SP, 05314-970, Brazil<sup>28</sup> Observatório Nacional, Rua Gal. José Cristino 77, Rio de Janeiro, RJ—20921-400, Brazil<sup>29</sup> National Center for Supercomputing Applications, 1205 West Clark St., Urbana, IL 61801, USA; [mcarras2@illinois.edu](mailto:mcarras2@illinois.edu)<sup>30</sup> Department of Astronomy, University of Illinois at Urbana-Champaign, 1002 W. Green Street, Urbana, IL 61801, USA

- <sup>31</sup> Institute of Space Sciences (ICE, CSIC), Campus UAB, Carrer de Can Magrans, s/n, E-08193 Barcelona, Spain  
<sup>32</sup> Institut d'Estudis Espacials de Catalunya (IEEC), E-08193 Barcelona, Spain  
<sup>33</sup> Kavli Institute for Cosmological Physics, University of Chicago, Chicago, IL 60637, USA  
<sup>34</sup> Department of Physics, University of Michigan, Ann Arbor, MI 48109, USA  
<sup>35</sup> University of Nottingham, School of Physics and Astronomy, Nottingham NG7 2RD, UK  
<sup>36</sup> Centro de Investigaciones Energéticas, Medioambientales y Tecnológicas (CIEMAT), Madrid, Spain; [nsevilla@gmail.com](mailto:nsevilla@gmail.com)  
<sup>37</sup> George P. and Cynthia Woods Mitchell Institute for Fundamental Physics and Astronomy, and Department of Physics and Astronomy, Texas A&M University, College Station, TX 77843, USA  
<sup>38</sup> Department of Physics, IIT Hyderabad, Kandi, Telangana 502285, India  
<sup>39</sup> Excellence Cluster Universe, Boltzmannstr. 2, D-85748 Garching, Germany  
<sup>40</sup> Faculty of Physics, Ludwig-Maximilians-Universität, Scheinerstr. 1, D-81679 Munich, Germany  
<sup>41</sup> Observatories of the Carnegie Institution of Washington, 813 Santa Barbara St., Pasadena, CA 91101, USA  
<sup>42</sup> Department of Astronomy/Steward Observatory, 933 North Cherry Avenue, Tucson, AZ 85721-0065, USA  
<sup>43</sup> Jet Propulsion Laboratory, California Institute of Technology, 4800 Oak Grove Dr., Pasadena, CA 91109, USA  
<sup>44</sup> Department of Physics, The Ohio State University, Columbus, OH 43210, USA  
<sup>45</sup> Department of Astronomy, University of Michigan, Ann Arbor, MI 48109, USA  
<sup>46</sup> Department of Astronomy and Astrophysics, University of California, Santa Cruz, CA 95064, USA  
<sup>47</sup> Universitäts-Sternwarte, Fakultät für Physik, Ludwig-Maximilians Universität München, Scheinerstr. 1, D-81679 München, Germany  
<sup>48</sup> Lawrence Berkeley National Laboratory, 1 Cyclotron Road, Berkeley, CA 94720, USA  
<sup>49</sup> Department of Astronomy, University of California, Berkeley, 501 Campbell Hall, Berkeley, CA 94720, USA  
<sup>50</sup> Santa Cruz Institute for Particle Physics, Santa Cruz, CA 95064, USA  
<sup>51</sup> Max Planck Institute for Extraterrestrial Physics, Giessenbachstrasse, D-85748 Garching, Germany  
<sup>52</sup> Harvard-Smithsonian Center for Astrophysics, Cambridge, MA 02138, USA  
<sup>53</sup> Department of Astronomy and Astrophysics, University of Chicago, Chicago, IL 60637, USA  
<sup>54</sup> Australian Astronomical Observatory, North Ryde, NSW 2113, Australia  
<sup>55</sup> Institute for Astronomy, University of Edinburgh, Edinburgh EH9 3HJ, UK  
<sup>56</sup> Department of Astronomy, The Ohio State University, Columbus, OH 43210, USA  
<sup>57</sup> Department of Physics, University of Arizona, Tucson, AZ 85721, USA  
<sup>58</sup> Department of Astrophysical Sciences, Princeton University, Peyton Hall, Princeton, NJ 08544, USA  
<sup>59</sup> Institució Catalana de Recerca i Estudis Avançats, E-08010 Barcelona, Spain  
<sup>60</sup> Department of Astronomy & Astrophysics, University of Toronto, Toronto, ON M5S 2H4, Canada  
<sup>61</sup> Jodrell Bank Center for Astrophysics, School of Physics and Astronomy, University of Manchester, Oxford Road, Manchester, M13 9PL, UK  
<sup>62</sup> Instituto de Física, UFRGS, Caixa Postal 15051, Porto Alegre, RS—91501-970, Brazil  
<sup>63</sup> INAF-Osservatorio Astronomico di Trieste, via G.B. Tiepolo 11, I-34131, Trieste, Italy  
<sup>64</sup> Brookhaven National Laboratory, Bldg. 510, Upton, NY 11973, USA  
<sup>65</sup> School of Physics and Astronomy, University of Southampton, Southampton, SO17 1BJ, UK  
<sup>66</sup> Austin Peay State University, Dept. Physics-Astronomy, P.O. Box 4608 Clarksville, TN 37044, USA  
<sup>67</sup> Department of Physics, Brandeis University, Waltham, MA 02453, USA  
<sup>68</sup> Instituto de Física Gleb Wataghin, Universidade Estadual de Campinas, 13083-859, Campinas, SP, Brazil  
<sup>69</sup> Korea Astronomy and Space Science Institute, Yuseong-gu, Daejeon, 305-348, Republic of Korea  
<sup>70</sup> Computer Science and Mathematics Division, Oak Ridge National Laboratory, Oak Ridge, TN 37831, USA  
<sup>71</sup> Department of Physics, University of Illinois at Urbana-Champaign, 1110 W. Green St., Urbana, IL 61801, USA  
<sup>72</sup> National Optical Astronomy Observatory, 950 North Cherry Avenue, Tucson, AZ 8571, USA  
<sup>73</sup> Department of Physics, Montana State University, P.O. Box 173840, Bozeman, MT 59717-3840, USA

Received 2018 January 17; revised 2018 September 20; accepted 2018 October 19; published 2018 November 26

## Abstract

We describe the first public data release of the Dark Energy Survey, DES DR1, consisting of reduced single-epoch images, co-added images, co-added source catalogs, and associated products and services assembled over the first 3 yr of DES science operations. DES DR1 is based on optical/near-infrared imaging from 345 distinct nights (2013 August to 2016 February) by the Dark Energy Camera mounted on the 4 m Blanco telescope at the Cerro Tololo Inter-American Observatory in Chile. We release data from the DES wide-area survey covering  $\sim 5000 \text{ deg}^2$  of the southern Galactic cap in five broad photometric bands, *grizY*. DES DR1 has a median delivered point-spread function of  $g = 1.12$ ,  $r = 0.96$ ,  $i = 0.88$ ,  $z = 0.84$ , and  $Y = 0''.90$  FWHM, a photometric precision of  $<1\%$  in all bands, and an astrometric precision of  $151 \text{ mas}$ . The median co-added catalog depth for a  $1''.95$  diameter aperture at signal-to-noise ratio  $(S/N) = 10$  is  $g = 24.33$ ,  $r = 24.08$ ,  $i = 23.44$ ,  $z = 22.69$ , and  $Y = 21.44 \text{ mag}$ . DES DR1 includes nearly 400 million distinct astronomical objects detected in  $\sim 10,000$  co-add tiles of size  $0.534 \text{ deg}^2$  produced from  $\sim 39,000$  individual exposures. Benchmark galaxy and stellar samples contain  $\sim 310$  million and  $\sim 80$  million objects, respectively, following a basic object quality selection. These data are accessible through a range of interfaces, including query web clients, image cutout servers, jupyter notebooks, and an interactive co-add image visualization tool. DES DR1 constitutes the largest photometric data set to date at the achieved depth and photometric precision.

**Key words:** astronomical databases: miscellaneous – catalogs – cosmology: observations – surveys – techniques: image processing – techniques: photometric

## 1. Introduction

Advances in telescope construction, sensor technology, and data processing have allowed us to map the sky with increasing speed and precision, enabling discovery through statistical

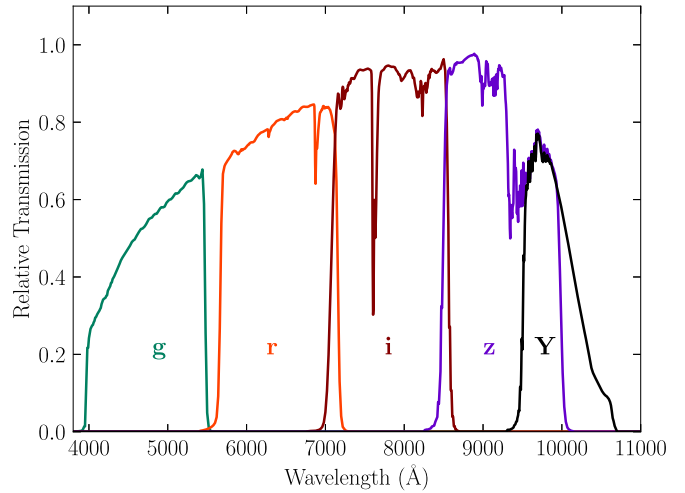
<sup>74</sup> Visitor at Kavli Institute for Cosmology, University of Cambridge, Madingley Road, Cambridge CB3 0HA.

analysis of astronomical source populations, as well as the detection of rare and/or unexpected objects (Tyson 2010). The Dark Energy Survey (DES) is one of several ground-based wide-area optical and near-IR imaging surveys, including the Sloan Digital Sky Survey (SDSS; York et al. 2000), the Panoramic Survey Telescope and Rapid Response System 1 (Pan-STARRS1 or PS1; Kaiser et al. 2010), the Kilo Degree Survey (KiDS; de Jong et al. 2013), the Hyper Suprime-Cam Subaru Strategic Program (HSC-SSP; Aihara et al. 2018a), and the future Large Synoptic Survey Telescope (LSST; Ivezić et al. 2008).

The instrumental and observational strategies of DES are designed to improve our understanding of cosmic acceleration and the nature of dark energy using four complementary methods: weak gravitational lensing, galaxy cluster counts, the large-scale clustering of galaxies (including baryon acoustic oscillations), and the distances to Type Ia supernovae (SNe; DES Collaboration 2005). To achieve these goals, DES conducts two distinct multiband imaging surveys: a  $\sim 5000 \text{ deg}^2$  wide-area survey in the *grizY* bands and a  $\sim 27 \text{ deg}^2$  deep SN survey observed in the *griz* bands with a  $\sim 7$ -day cadence (Diehl et al. 2014; Kessler et al. 2015).

DES uses the Dark Energy Camera (DECam; Honscheid et al. 2008; Flaugher et al. 2015), a 570 MP camera with a  $3 \text{ deg}^2$  field of view installed at the prime focus of the Blanco 4 m telescope at the Cerro Tololo Inter-American Observatory (CTIO) in northern Chile. Survey observations comprise  $\sim 105$  equivalent full nights per year (August through mid-February), including full and half nights. Each exposure is delivered from CTIO to the National Center for Supercomputing Applications (NCSA) at the University of Illinois at Urbana-Champaign for processing generally within minutes of being observed. At NCSA, the DES Data Management system (DESDM; Sevilla et al. 2011; Desai et al. 2012; Mohr et al. 2012; Morganson et al. 2018) generates a variety of scientific products, including single-epoch and co-added images with associated source catalogs of suitable quality to perform precise cosmological measurements (e.g., DES Collaboration 2017).

Raw DES exposures become publicly available 1 yr after acquisition from the National Optical Astronomy Observatory (NOAO) Science Archive,<sup>75</sup> and DES is scheduled to provide two major public releases of processed data. The first DES Data Release (DR1), described here, encompasses data products derived from wide-area survey observations taken in the first 3 yr of science operations (Y1–Y3, from 2013 August to 2016 February). A second major data release (DR2) is scheduled for after DES is completed. In addition to DR1 and DR2, the DES Collaboration prepares incremental internal releases with value-added products and detailed characterizations of survey performance that are designed to support cosmological analyses (e.g., Y1 Gold; Drlica-Wagner et al. 2018). A subset of these products associated with data collected during the DES Science Verification (SV) period (2012 November 1 through 2013 February 22) was released in 2016 January.<sup>76</sup> In 2018 September, the value-added products from a number of selected DES publications corresponding to Y1 data were released as well.<sup>77</sup> Additional releases of value-added data products are expected to support future scientific publications.



**Figure 1.** DR1 standard bandpasses for the DECam *grizY* filters. The bandpasses represent the total system throughput, including atmospheric transmission (air mass = 1.2) and the average instrumental response across the science CCDs (Section 5.4).

In this work, we present the content, validation, and data access services for DES DR1. DR1 is composed of co-added images and catalogs, as well as calibrated single-epoch images, from the processing of the first 3 yr of DES wide-area survey observations. Access to DES DR1 data is provided via web interfaces and auxiliary tools, which is made possible through the partnership between NCSA,<sup>78</sup> LineA,<sup>79</sup> and NOAO,<sup>80</sup> at the following URL: <https://des.ncsa.illinois.edu/releases/dr1>. In Section 2, we briefly describe the DECam instrument and the DES observation strategy for the wide-field survey (the data set included in this release). Section 3 includes an overview of how the raw data were processed by DESDM at NCSA and served as the catalogs and images made available in this release. A basic quality evaluation of these products is presented in Section 4, followed by a description of products as they appear in the DR1 release (Section 5). Section 6 describes the various data access frameworks and tools made available for DR1. A summary of the release and information on expected future releases are given in Section 7. We direct the reader to Appendix A for definitions of terms and acronyms used throughout the text.

Except where noted, all magnitudes quoted in the text are in the AB system (Oke 1974).

## 2. Data Acquisition

DR1 is composed of data taken on 345 distinct nights spread over the first 3 yr of DES operations from 2013 August 15 to 2016 February 12.<sup>81</sup> In this section, we briefly describe the characteristics of the DECam instrument and the DES observation strategy to provide context for DR1. We point the reader to other DES publications for further details on the technical aspects summarized here (i.e., Diehl et al. 2016; Drlica-Wagner et al. 2018; Morganson et al. 2018).

<sup>78</sup> National Center for Supercomputing Applications.

<sup>79</sup> Laboratório Interinstitucional de e-Astronomia.

<sup>80</sup> National Optical Astronomy Observatory.

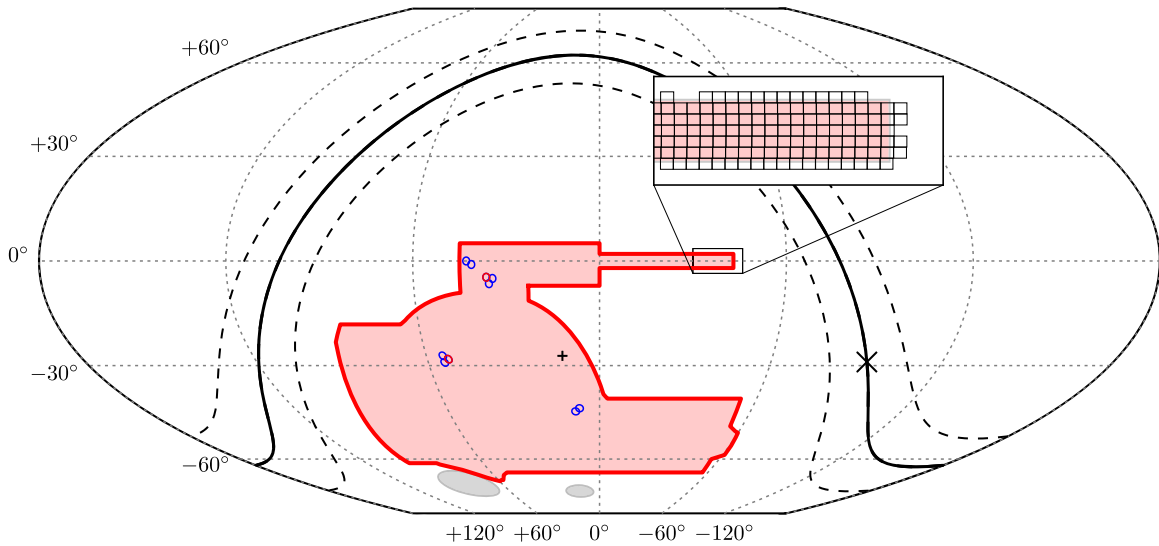
<sup>81</sup> DES was scheduled for 319 equivalent full nights, including half nights, during this period (Diehl et al. 2016).

<sup>75</sup> <http://archive.noao.edu/>

<sup>76</sup> <https://des.ncsa.illinois.edu/releases/sval>

<sup>77</sup> <https://des.ncsa.illinois.edu/releases/y1a1>





**Figure 2.** Plot of the DES survey area in celestial coordinates. The  $\sim 5000 \text{ deg}^2$  wide-area survey footprint is shown in red. The eight shallow SN fields are shown as blue circles, and the two deep SN fields are shown as red circles. The Milky Way plane is shown as a solid line, with dashed lines at  $b = \pm 10 \text{ deg}$ . The Galactic center (cross) and south Galactic pole (plus sign) are also marked. The Large and Small Magellanic Clouds are indicated in gray. The inset panel shows an overlay of co-add processing units, co-add tiles, on top of the SDSS Stripe 82 area. This and the other sky map plots included in this work use the equal-area McBryde–Thomas flat-polar quartic projection.

### 2.1. DECam

DECam is a wide-field-of-view ( $3 \text{ deg}^2$ ) mosaic camera containing 62 science CCDs (Flaugher et al. 2015).<sup>82</sup> The corrector system and pixel size provide an average plate scale of  $0''.263$  per pixel. The DES wide-area survey observes five broadband filters, *grizY* (Figure 1), and the standard bandpasses for these filters are included as part of DR1 (Section 5.4). The DES filters are very similar to their analogously named counterparts from other surveys.

Uniquely, the DES *z* band has greater sensitivity at longer wavelengths than the SDSS *z* band and overlaps with the DES *Y* band. Additional details, including construction, installation, and a description of DECam subsystems and interfaces, are provided in Flaugher et al. (2015).

### 2.2. Survey Operations

The target footprint of the DES wide-area and SN surveys are shown in Figure 2. All R.A., decl. coordinates in this paper refer to the J2000 epoch. The wide-area footprint shape was selected to obtain a large overlap with the South Pole Telescope survey (Carlstrom et al. 2011) and Stripe 82 from SDSS (Abazajian et al. 2009) and includes a connection region to enhance overall calibration. Given the cosmological goals of the survey, DES avoids the Galactic plane to minimize stellar foregrounds and extinction from interstellar dust.

The wide-field survey uses exposure times of 90 s for *griz* and 45 s for *Y* band, yielding a typical single-epoch point-spread function (PSF) depth at signal-to-noise ratio ( $S/N$ ) = 10 of  $g = 23.57$ ,  $r = 23.34$ ,  $i = 22.78$ ,  $z = 22.10$ , and  $Y = 20.69$  (Morganson et al. 2018). The completed survey is expected to be roughly 1 mag deeper, through the co-addition of 10 images in each of the bands for a cumulative exposure time of 900 s in *griz* and 450 s in *Y*.<sup>83</sup>

<sup>82</sup> Two and a half DECam CCDs have failed over the course of DES operation and are only included in DR1 when operating properly (Diehl et al. 2014; Flaugher et al. 2015; Morganson et al. 2018).

<sup>83</sup> Beginning in Y4, *Y*-band exposure times were increased to 90 s to reduce overhead while maintaining the same cumulative exposure target.

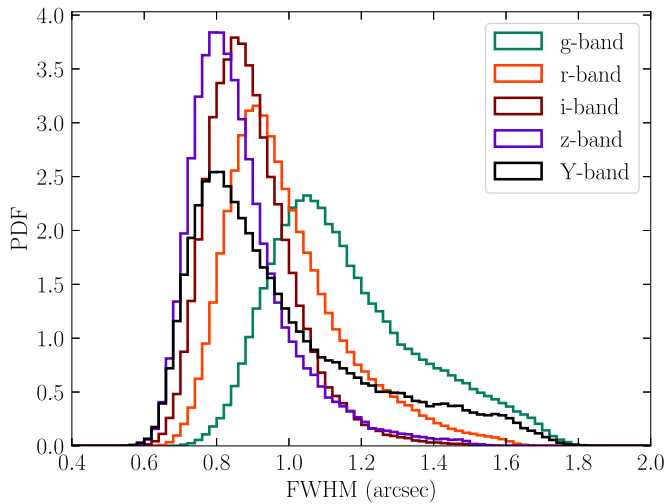
Nightly observations are divided between the wide-field and SN surveys based on current environmental conditions and the data quality assessments of previous observations. Real-time optimization of survey strategy is accomplished through the ObsTac software on the mountain (Neilsen & Annis 2014). ObsTac selects *grizY* exposures accounting for moon position, sky brightness, current seeing, air mass, hour angle, and other observational characteristics. DES exposures are offset by roughly half the focal plane radius on average in successive visits to the same field, or “hex,” such that objects are observed by different CCDs in each “tiling.” This observing strategy minimizes inhomogeneities from the DECam geometry and enhances the relative photometric calibration. Blanco is an equatorial mount telescope, and there is no rotation between dithered and/or repeated exposures.

A single raw DECam exposure is  $\sim 0.5 \text{ GB}$  in size (compressed), and DES collects  $\sim 300$  science exposures per night, depending on the season, survey strategy, and SN field schedule. These data are transferred to NOAO for archiving (Fitzpatrick 2010; Honscheid et al. 2012) and to NCSA for further evaluation and processing by the DESDM system; a summary is provided in Section 3. These raw single-epoch images are made available by NOAO and are accessible as described in Section 6.

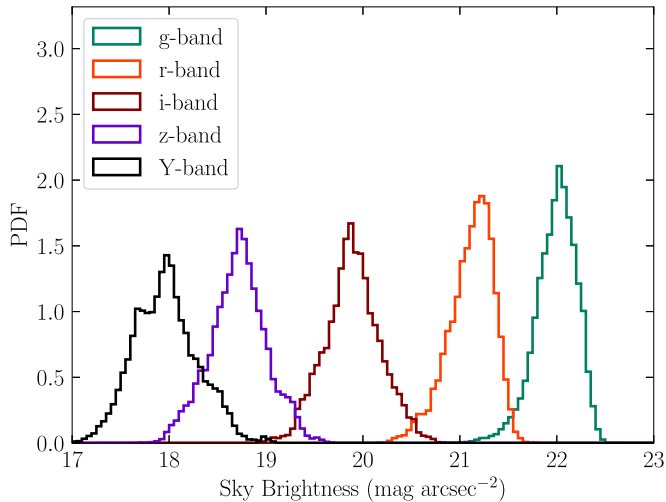
### 2.3. Survey Progress through DR1

Between Y1 and Y3, 38,850 wide-field exposures passed baseline survey-quality thresholds based on effective exposure time and PSF FWHM (Morganson et al. 2018, Section 4.7) and are included in co-add processing by DESDM (Morganson et al. 2018). The median air mass of DR1 survey-quality exposures was 1.22, with  $>99\%$  of exposures taken at air mass  $<1.4$ . Meanwhile, the median delivered seeing (FWHM) was  $g = 1.12$ ,  $r = 0.96$ ,  $i = 0.88$ ,  $z = 0.84$ , and  $Y = 0''.90$  (Figure 3). Note that ObsTac prioritizes observations in the *riz* bands during periods of good seeing to advance the main science goals of DES (e.g., cosmological constraints from weak gravitational lensing). Figure 4 shows the distribution of sky





**Figure 3.** Normalized histograms showing the distribution of PSF FWHM for single-epoch images that form the DR1 co-add.

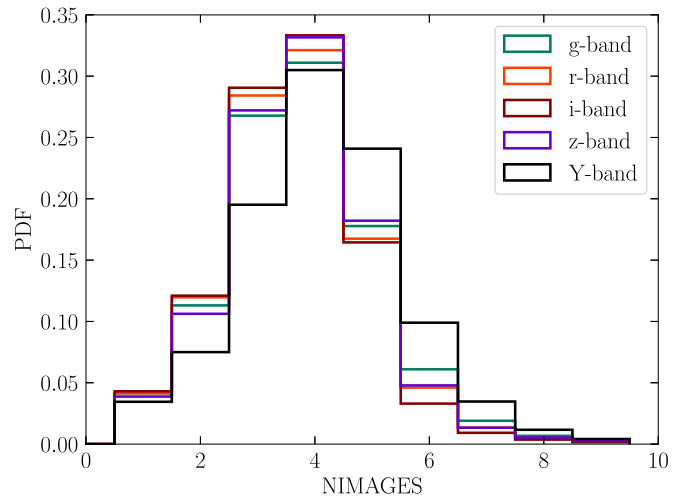


**Figure 4.** Normalized histograms showing the distribution of sky brightness for single-epoch images that form the DR1 co-add. All magnitudes are given in the AB system.

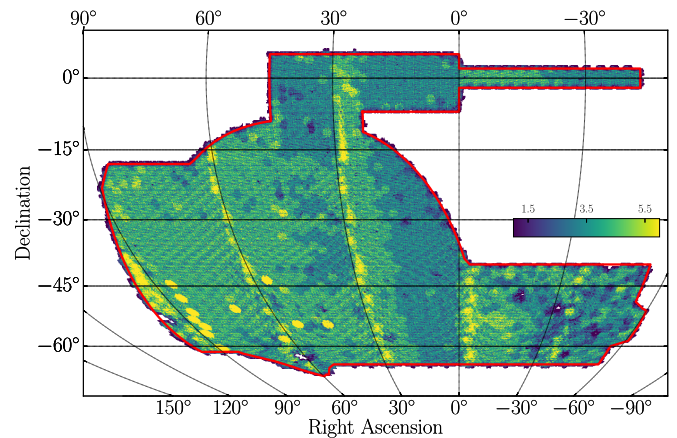
brightness levels for single-epoch images; the median sky brightness is  $g = 22.01$ ,  $r = 21.15$ ,  $i = 19.89$ ,  $z = 18.72$ , and  $Y = 17.96$  mag arcsec<sup>-2</sup>. The resulting median single-epoch effective image noise level (square root of the calibrated image variance), including additional contributions from read noise and shot noise of the dome flat, is  $g = 25.25$ ,  $r = 24.94$ ,  $i = 24.31$ ,  $z = 23.58$ , and  $Y = 22.28$  mag arcsec<sup>-2</sup>.

Each position in the DES DR1 footprint is typically covered by three to five overlapping DECam exposures in each of the *grizY* bands (Figure 5). As an example, a map for the number of overlapping *i*-band exposures across the footprint is shown in Figure 6.

The total sky coverage of DR1 was estimated using maps of the individual image coverage generated by *mangle* (Hamilton & Tegmark 2004; Swanson et al. 2008) and converted to HEALPix (Górski et al. 2005) maps with spatial resolution comparable to the size of gaps between individual CCDs ( $n_{\text{side}} = 4096$ ,  $\sim 0.86$ ; Drlica-Wagner et al. 2018). When requiring at least one exposure in a given band, the areal coverage of each individual band is  $g = 5224$ ,  $r = 5231$ ,  $i = 5230$ ,  $z = 5234$ , and  $Y = 5227$  deg<sup>2</sup>. When requiring



**Figure 5.** Histograms showing the distribution of overlapping images in each of the *grizY* bands normalized over the DR1 footprint. Most regions of the footprint are covered with three to five images.



**Figure 6.** Map of the DES footprint showing the number of overlapping *i*-band exposures. Regions of above-average coverage are a consequence of the DES hexagonal layout scheme and can be found at intervals of  $\Delta \text{R.A.} = 30^\circ$ . Color range units are number of exposures.

at least one exposure in all of the *grizY* bands, the DR1 footprint area is 5186 deg<sup>2</sup>. These areal coverage numbers do not account for regions that are masked around bright stars or masked owing to other imaging artifacts, which decrease the areal coverage by  $\sim 200$  deg<sup>2</sup>. Note also that we are not releasing *mangle* products for DR1. Instead, we are providing HEALPix indices for all the objects at different resolutions, as well as a tabulated HEALPix map with  $n_{\text{side}} = 32$  for the footprint. See Section 6 for more details about these products.

### 3. Data Release Processing

We briefly describe the DESDM processing pipeline applied to the DES data to generate the DR1 data products.<sup>84</sup> DR1 is based on the DESDM Y3A2 internal release to the DES Collaboration, referring to the second annual release of data products obtained from the first three seasons of DES science operations and the Science Verification period. Where possible,

<sup>84</sup> Note that the DESDM pipeline differs from the DECam community pipeline.

our pipelines use the *AstrOmatic*<sup>85</sup> suite of tools to perform standard tasks (Bertin & Arnouts 1996; Bertin et al. 2002; Bertin 2006, 2010, 2011). A full description of the pipeline and the underlying image detrending algorithms can be found in Morganson et al. (2018) and Bernstein et al. (2017a).

### 3.1. Single-epoch Processing

The DES single-epoch processing pipeline (known as “Final Cut”) removes instrumental signatures to produce reduced, science-ready images (Morganson et al. 2018). Final Cut performs overscan removal, cross-talk correction, nonlinearity correction, bias subtraction, gain correction, correction for the brighter-fatter effect (Gruen et al. 2015), bad-pixel masking, astrometric matching, flagging of saturated pixels and bleed trails, principal-component background subtraction, secondary flat-field correction, and the masking of cosmic rays and other imaging artifacts. The resulting images from this pipeline form the products that are released through the NOAO Science Archive.<sup>86</sup> Those images are provided in FITS-formatted files and contain extensions for the science data (SCI), an inverse-variance weight (WGT), and a mask of bad pixels (MSK). Note that the weight plane is not altered to account for flagged defects; this allows the user to customize the severity of the defects to be removed based on their own analysis needs. A summary of the flags available is provided in Table 9 of Morganson et al. (2018).

Final Cut also performs PSF model fitting with *PSFEX* (Bertin 2011) and source detection and measurement with *SExtractor* (Bertin & Arnouts 1996). These single-epoch data products are not part of DR1.

### 3.2. Multi-epoch (Co-add) Processing

The multi-epoch pipeline produces co-added images and catalogs of astronomical objects (Morganson et al. 2018). The co-add processing is organized within a tiling scheme that subdivides the sky into square regions with  $0^{\circ}.7306$  on a side. Co-add images are  $10,000 \times 10,000$  pixels with a pixel scale of  $0''.263$ . The choice of images that are tendered as inputs to this pipeline is based on the data quality assessment that occurred in the Final Cut pipeline and the Forward Global Calibration Method (FGCM) for photometric calibration (Burke et al. 2018). In addition, a “blacklist” of images with severe scattered light, ghosts, or bright transient defects (e.g., comets, meteors, and airplanes) is used to exclude additional images from co-add processing. The co-added images are rescaled such that the zero-point is fixed to 30 for all filters. This makes the conversion between flux and magnitude the same for all bands.

The multi-epoch pipeline begins by refining the astrometric solution for the image inputs. This step operates on catalog objects from all input images in all bands simultaneously to provide a consistent alignment between images. The relative astrometry within a tile has a typical rms residual of 30 mas or better. During this process, the absolute astrometry is tied to the Two Micron All Sky Survey (2MASS; Skrutskie et al. 2006).<sup>87</sup>

The next step prepares the images for co-addition. First, the World Coordinate System (WCS; Calabretta & Greisen 2002; Greisen & Calabretta 2002) information for each image is

updated to reflect the astrometric shifts solved in the previous step. Then a pair of weight planes are formed, which set the as-yet unaltered single-epoch weights to zero to remove defects tracked in the MSK plane. Both weight planes are formed so that we can separately track spatially persistent defects (e.g., saturated stars and bleed trails) and temporary defects (e.g., interpolated bad columns, cosmic rays, satellite trails). The first weight plane contains all defects, while the second weight plane contains only the persistent defects. The *AstrOmatic* utility *SWarp* (Bertin et al. 2002) is then used to form the co-add image (SCI) and weight (WGT) planes; the former uses the first weight plane, while the latter uses the second. A mask plane (MSK) is formed that carries a value of 0 for good pixels and 1 for pixels where no good data exist (due to lack of image coverage or persistent defects).

A subsequent execution of *SWarp* is then used to form a detection image that is a linear combination of the  $r + i + z$  bands using the “CHI-MEAN” weighting (Drlica-Wagner et al. 2018, Appendix B), and *PSFEX* is used to obtain a PSF model for each tile. Initial catalogs are constructed using *SExtractor* in dual-image mode where the detection image is used to form the segmentation map of sources prior to extracting measurements from the individual co-add images. We caution that the PSF model is unable to fully account for discontinuities that occur at image boundaries. This limits the precision of the measurements of quantities such as *MAG\_PSF* to no better than a few percent. In addition, morphological classifiers based on the co-add PSF model, such as *CLASS\_STAR* and *SPREAD\_MODEL*, can have a degraded/varied performance.

To provide a solution that overcomes most of the limitations of the co-add catalog products, the single-epoch catalogs are matched to the co-add detection catalog, and weighted averages of the single-epoch *MAG\_PSF* and *SPREAD\_MODEL* measurements are made from all unflagged detections of the same object for each band. We add the *WAVG\_* prefix to indicate these weighted-average quantities (Morganson et al. 2018).

These weighted-average measurements are included among the public data release products. Longer term, the DES Collaboration is pursuing improved photometry through the use of multi-epoch, multiband, and multi-object fitting that operates on the Final Cut single-epoch images (Drlica-Wagner et al. 2018). Those products are maturing but are beyond the scope of the current public data release. They should become available along with the results from the DES Y3 cosmology analyses.

## 4. Data Quality

In this section, we provide a general assessment of the DR1 data quality, including astrometric and photometric precision, imaging depth in terms of measurement S/N and object detection completeness, morphological object classification accuracy, and the identification and removal of likely artifacts. A summary of data quality metrics is found in Table 1.

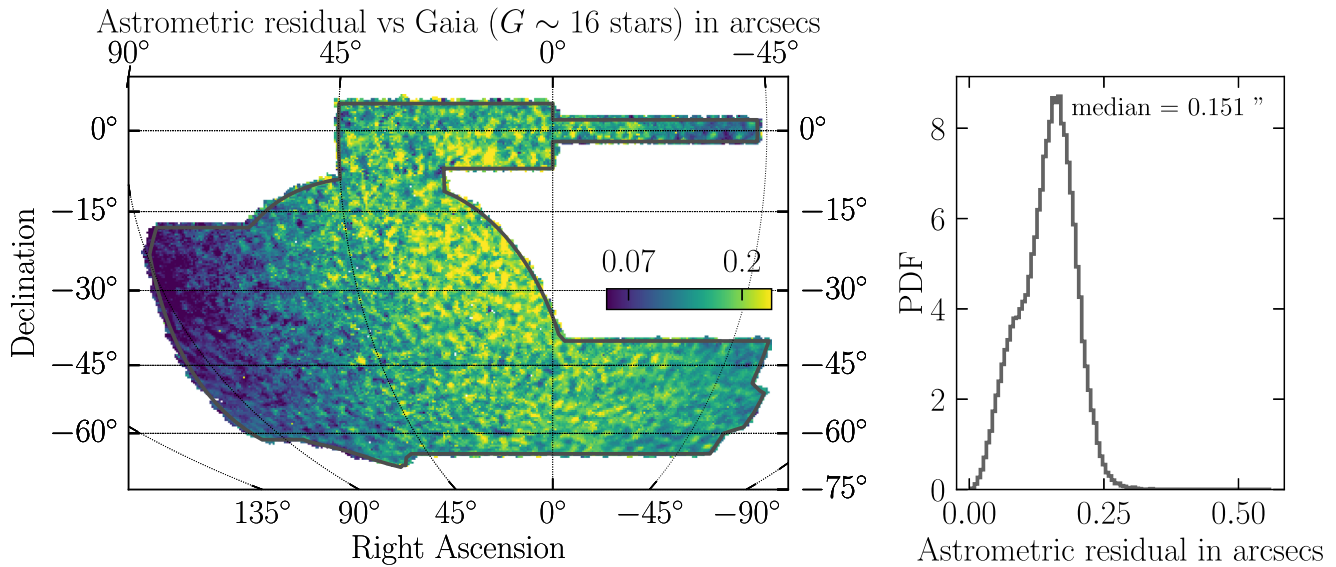
### 4.1. Astrometry

The DR1 astrometric solution is derived in two steps using *SCAMP* with 2MASS as the reference catalog (Morganson et al. 2018). At the single-epoch stage, we find internal astrometric uncertainties of  $g = 42$ ,  $r = 36$ ,  $i = 37$ ,  $z = 39$ , and  $Y = 56$  mas, as determined from the median of 2D

<sup>85</sup> <https://www.astromatic.net/>

<sup>86</sup> <http://archive.noao.edu/>

<sup>87</sup> The *Gaia* data releases were not yet available when the processing began.



**Figure 7.** Absolute astrometric precision (total distance) measured relative to stars in Gaia DR1 with  $G$ -band magnitude,  $G_{\text{Gaia}} \sim 16$  (Jordi et al. 2010). Left: mean value of the astrometric discrepancy with respect to *Gaia* vs. sky position computed within HEALPix cells of resolution  $n_{\text{side}} = 256$ . Right: normalized histogram showing the distribution of astrometric offsets. Color range units are in arcseconds.

**Table 1**  
DES DR1 Key Numbers and Data Quality Summary

Parameter	Band					Reference
	$g$	$r$	$i$	$z$	$Y$	
Number of exposures in co-add	7626	7470	7470	7753	8531	Section 2
Single-epoch PSF FWHM (arcsec)	1.12	0.96	0.88	0.84	0.90	Section 2.3
Single-epoch sky brightness (mag arcsec <sup>-2</sup> )	22.01	21.15	19.89	18.72	17.96	Section 2.3
Single-epoch effective image noise <sup>a</sup> (mag arcsec <sup>-2</sup> )	25.25	24.94	24.31	23.58	22.28	Section 2.3
Sky coverage (individual bands, deg <sup>2</sup> )	5224	5231	5230	5234	5227	Section 2.3
Sky coverage ( <i>grizY</i> intersection, deg <sup>2</sup> )			5186			Section 2.3
Single-epoch astrometric repeatability (total distance, mas)	42	36	37	39	56	Section 4.1
Co-add astrometric precision (total distance, mas)		30 (internal); 151 (versus <i>Gaia</i> )				Section 4.1
Absolute photometric statistical uncertainty <sup>b</sup> (mmag)	2.6	2.9	3.4	2.5	4.5	Section 4.2
Single-epoch photometric repeatability (mmag)	7.3	6.1	5.9	7.3	7.8	Section 4.2
Co-add photometric precision (mmag)	5	4	4	5	5	Section 4.2
Co-add photometric uniformity versus <i>Gaia</i> (mmag)		6.6		...	...	Section 4.2
Single-epoch magnitude limit (PSF, S/N = 10)	23.57	23.34	22.78	22.10	20.69	Section 2.2
Co-add magnitude limit (MAG_APER_4, 1.95 arcsec diameter, S/N = 10)	24.33	24.08	23.44	22.69	21.44	Section 4.4
Co-add 95% completeness limit (mag)	23.72	23.35	22.88	22.25	...	Section 4.4
Co-add spurious object rate			$\lesssim 1\%$			Section 4.4
Co-add galaxy selection (EXTENDED_COADD $\geq 2$ , MAG_AUTO_I $\leq 22.5$ )			Efficiency > 99%; Contamination < 3%			Section 4.5
Co-add stellar selection (EXTENDED_COADD $\leq 1$ , MAG_AUTO_I $\leq 22.5$ )			Efficiency > 90%; Contamination < 3%			Section 4.5

**Notes.** For parameters representing a distribution, the median or mean values are quoted as specified in the main text. All magnitudes are in the AB system.

<sup>a</sup> Square root of the calibrated image variance, including read noise.

<sup>b</sup> The *Hubble* CalSpec standard star C26202 is used as an absolute reference for the AB system.

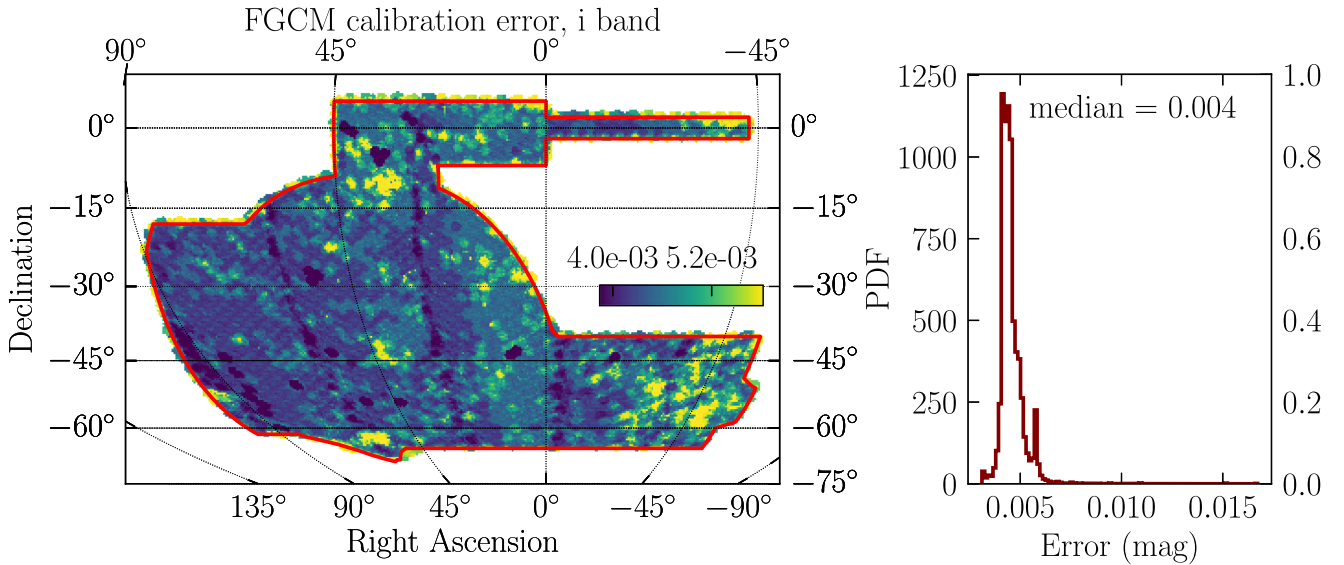
angular separations between repeated measurements of bright stars from individual exposures. Following the astrometric refinement step for image co-addition by SCAMP, the estimated internal astrometric precision for the co-add is  $\sim 30$  mas rms (median over co-add tiles, averaging all five bands). The absolute astrometric uncertainty of the co-add is evaluated with respect to *Gaia* DR1 (Gaia Collaboration et al. 2016). Figure 7 shows that the 2D astrometric residuals are smallest in regions with larger stellar densities closer to the Galactic plane (for comparison, see Figure 14), and the median over the footprint is  $\sim 151$  mas. Further details of astrometric calibration,

including ongoing development using *Gaia* as a reference catalog, are provided in Bernstein et al. (2017b).

#### 4.2. Photometry

The relative standard bandpass flux measurements for astronomical sources in DR1 have been calibrated using a forward modeling technique to account for both atmospheric and instrumental components of the total system throughput (FGCM; Burke et al. 2018). The parameters of the model were initially fit from observations taken in photometric conditions to establish a network of calibration stars that spans the full





**Figure 8.** Statistical uncertainty of co-add zero-points in the  $i$  band estimated from the FGCM photometric calibration. Left: mean value of the uncertainty vs. sky position, computed within HEALPix cells of resolution  $n_{\text{side}} = 256$ . Right: normalized histogram showing the distribution of zero-point uncertainties over the footprint. Color range units are in AB magnitudes.

survey footprint. This network was subsequently used to refine the calibration of exposures taken in nonphotometric conditions. Meanwhile, the absolute photometric calibration of DR1 is tied to the spectrophotometric *Hubble* CALSPEC standard star C26202 (Bohlin et al. 2014) located in the SN field C3.

Over 100 repeated measurements of C26202 in a variety of conditions yielded a set of small shifts ( $\sim 3$  mmag) to place the DES photometry on the AB system. These shifts have been pre-applied to the DR1 zero-points. The statistical uncertainty on these shifts is estimated to be  $g = 2.6$ ,  $r = 2.9$ ,  $i = 3.4$ ,  $z = 2.5$ , and  $Y = 4.5$  mmag. Additional sources of systematic uncertainty on the absolute photometric calibration could arise from uncertainty in the level of out-of-band light leakage and uncertainty in the synthetic photometry of C26202. We are currently undertaking observations and analysis of two additional *HST* CALSPEC standards to reduce the systematic uncertainty of the AB offsets.

We reproduce below several of the key results from Burke et al. (2018) regarding the relative photometric calibration. The single-epoch photometric statistical precision (associated with random errors in the FGCM fit parameters) derived from repeated measurements of FGCM calibration stars is  $g = 7.3$ ,  $r = 6.1$ ,  $i = 5.9$ ,  $z = 7.3$ , and  $Y = 7.8$  mmag. Under the assumption that successive tiled observations of the same fields yield largely independent model fit parameters (as would be expected from the widely spaced observations in DES), we estimate the statistical precision of co-add zero-points by combining the fit results from overlapping exposures. The median co-add zero-point statistical uncertainty is  $g = 5$ ,  $r = 4$ ,  $i = 4$ ,  $z = 5$ , and  $Y = 5$  mmag. Figure 8 shows an example distribution for the  $i$  band. As a validation, we compare the photometric uniformity of DES DR1 to the space-based *Gaia*  $G$ -band photometry (Figure 9). Variations in uniformity are found to be 6.6 mmag, as estimated from a Gaussian fit to the offset distribution between  $G_{\text{Gaia}}$  and  $G_{\text{pred}}(r)$  predicted from the DES  $r$  band (Appendix B).

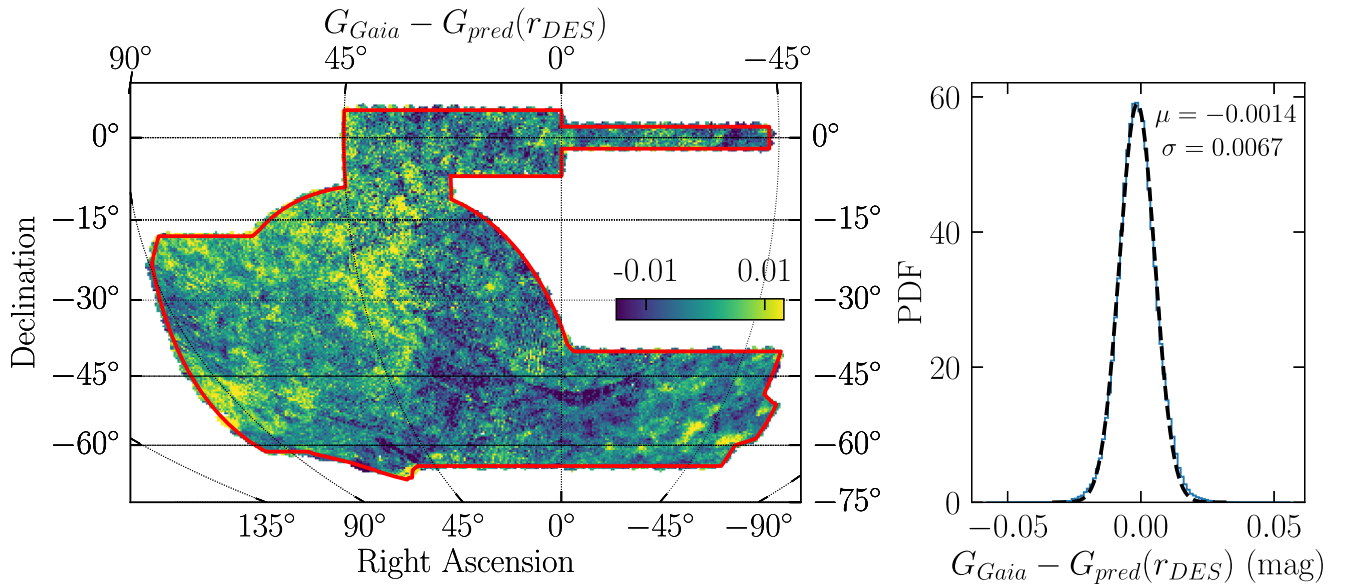
To account for extinction from interstellar dust, we include an additional column in the DR1 photometry tables for  $E(B - V)$  values from the reddening map of

Schlegel et al. (1998, hereafter SFD98) at the location of each catalog object. The  $E(B - V)$  values were obtained using a linear interpolation of the zenithal equal-area projected map distributed by SFD98. We computed fiducial interstellar extinction coefficients,  $R_b$ , for each band so that the corrections to the FGCM calibrated source magnitudes are  $A_b = E(B - V)R_b$ . Fiducial coefficients are derived using the Fitzpatrick (1999) reddening law with  $R_V = 3.1$  and the Schlafly & Finkbeiner (2011) calibration adjustment to the original SFD98 reddening map ( $N = 0.78$ ). Note that the Schlafly & Finkbeiner (2011) calibration adjustment is included in our fiducial reddening coefficients; these coefficients are intended to be used directly with  $E(B - V)$  values from the original SFD98 reddening map. We integrate over the DR1 standard bandpasses (Section 5.4) considering a fixed source spectrum that is constant in spectral flux density per unit wavelength,  $f_\lambda$  ( $\text{erg cm}^{-2} \text{s}^{-1} \text{\AA}^{-1}$ ), and adopted the low-extinction limit. The latter simplification is appropriate for DES, for which  $E(B - V) < 0.1$  mag over  $\sim 99\%$  of the footprint. The resulting multiplicative coefficient for each band is  $R_g = 3.186$ ,  $R_r = 2.140$ ,  $R_i = 1.569$ ,  $R_z = 1.196$ , and  $R_Y = 1.048$ . The DES science team continues to explore systematic uncertainties associated with interstellar extinction modeling.

In general, the photometry columns included in the DR1 database tables are not dereddened by default. However, the DR1\_MAIN table includes additional columns for the dereddened versions of MAG\_AUTO and WAVG\_MAG\_PSF indicated by a \_DERED suffix (Appendix E).

#### 4.3. Flagged Objects

For co-add objects, if any pixel is masked in all of the contributing exposures for a given band, the IMAFLAG-S\_ISO = 1 flag is set for that band. This flag is predominantly set for saturated objects and objects with missing data. We recommend a baseline quality criterion of IMAFLAG-S\_ISO = 0 (in the relevant bands) for most science applications since the majority of flagged objects have unreliable photometry. The DES DR1 catalog also includes other standard



**Figure 9.** Distribution of photometric residuals against Gaia’s  $G$  band (mag units) across the DES footprint used to evaluate the uniformity of the co-add FGCM calibration. Left: mean value of this residual vs. sky position in a HEALPix cell of  $n_{\text{side}} = 256$ . Right: normalized histogram of photometric residuals over the footprint. Color range units are in AB magnitudes.

**Table 2**  
DES DR1 Co-add Catalog Median Depth Estimates for the Sample of All High-quality Objects

Method	Band				
	$g$	$r$	$i$	$z$	$Y$
Maximum in number counts (MAG_AUTO)	24.32	23.89	23.41	22.09	21.40
Measured with $S/N = 10$ (MAG_AUTO)	23.52	23.10	22.51	21.81	20.61
Measured with $S/N = 10$ (MAG_APER_4)	24.33	24.08	23.44	22.69	21.44
Imaging depth from <i>mangle</i> (MAG_APER_4)	24.282	23.952	23.335	22.628	21.383
Detection completeness of 95% (MAG_AUTO)	23.72	23.35	22.88	22.25	...

**Note.** All magnitudes are given in the AB system.

flags `FLAGS` provided by the `SExtractor` pipeline. A summary of `SExtractor` `FLAGS` bitmask values and warning descriptions is provided in Appendix D.

#### 4.4. Depth

The effective depth of the DES DR1 wide-field co-add catalog is dependent on the photometric measurement of interest and can be quantified through various approaches. Here we derive simple depth estimates from the flux distribution of cataloged objects, the magnitude corresponding to a fixed  $S/N$  threshold ( $S/N = 10$ ), an aperture estimate from the input imaging, and object detection completeness. In general, the type of source and surface brightness must also be considered when evaluating the survey depth.

The settings used for the source extraction and deblending steps of the DESDM pipeline allow for efficient detection of objects with  $S/N \sim 10$  in the  $r + i + z$  composite detection image (Morganson et al. 2018). At the bright end, saturation effects start to become important at  $r < 16$ . For even brighter magnitudes, the fraction of saturated objects increases until objects are no longer cataloged owing to pixel-level masking applied during processing. For each of the depth studies considered here, we selected a sample of high-quality DR1 co-add objects using `FLAGS_[GRIZ] < 4` and `IMAFLAGS_ISO_[GRIZ] = 0`. No star-galaxy selection has been applied to the

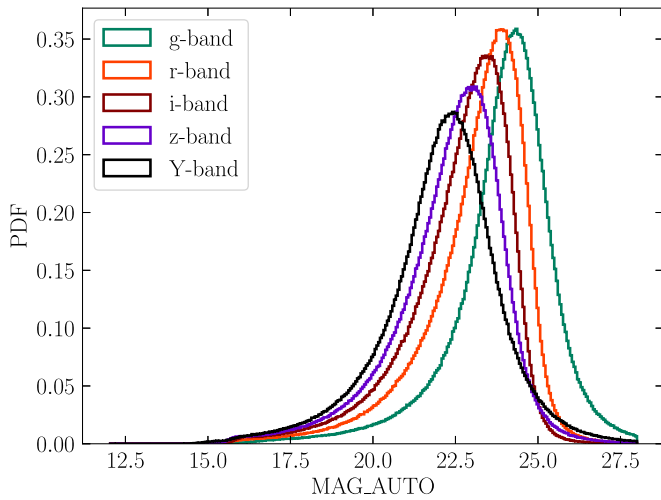
sample of analyzed objects. Below we describe these different approaches to estimate the depth of DR1; results from each method are provided in Table 2.

##### 4.4.1. Flux Distribution

The distribution of astronomical sources is weighted toward low-flux sources. A crude estimate of the detection threshold is given by the mode of the number count distribution of sources as a function of magnitude. Figure 10 shows the number counts of co-add objects as a function of `MAG_AUTO` in all five DES bands. The mode of the `MAG_AUTO` distribution is  $g = 24.32$ ,  $r = 23.89$ ,  $i = 23.41$ ,  $z = 22.09$ , and  $y = 21.40$ . No restrictions were placed on source morphology (i.e., stars vs. galaxies) for this estimate.

##### 4.4.2. Magnitude Limit at Fixed Signal-to-noise Ratio

The magnitude limit corresponding to a fixed  $S/N$  for a given photometric measurement (e.g., `MAG_AUTO`) can be empirically determined from the distribution of magnitude uncertainties as a function of magnitude (Rykoff et al. 2015). `SExtractor` provides an estimate of the photometric uncertainty through the `MAGERR` quantities, which are estimated from the fluctuations of the background around the sources. These are related to  $S/N$ ,  $\delta F/F$ , via the differentiation



**Figure 10.** Normalized histograms of source counts binned by SExtractor’s `MAG_AUTO` quantity showing the flux distribution of detected sources. All magnitudes are given in the AB system.

of Pogson’s law (Pogson 1856):

$$\delta m = \frac{-2.5 \delta F}{\ln 10 \frac{F}{F}}. \quad (1)$$

We summarize in Table 2 the characteristic  $S/N = 10$  thresholds for `MAG_AUTO` corresponding to  $\delta F/F \sim 0.1$  in each of the *grizY* bands. The left panel of Figure 11 shows the `MAG_AUTO` distribution for DES DR1 catalog objects with  $0.10837 < \text{magerr\_auto} < 0.10877$ . The spread in these distributions comes from the dependence of  $S/N$  on source properties (e.g., surface brightness) and survey nonuniformity.

#### 4.4.3. Depth from Image Properties

It is also possible to estimate the DES DR1 imaging depth using *mangle* (Hamilton & Tegmark 2004; Swanson et al. 2008), which generates a vectorized map of the survey coverage accounting for the focal plane geometry and imaging artifacts (i.e., bright star masks, bleed trails, satellite trails; Drlica-Wagner et al. 2018; Morganson et al. 2018). The *mangle* processing produces a co-add weight map from a weighted sum of the single-epoch input images. This weight was converted to an  $S/N = 10$  limiting magnitude for a  $2''$  diameter aperture, corresponding approximately to the `MAG_APER_4` quantity measured by SExtractor (for details, see Drlica-Wagner et al. 2018). The median limiting magnitude across the DES footprint is  $g = 24.282$ ,  $r = 23.952$ ,  $i = 23.335$ ,  $z = 22.628$ , and  $Y = 21.383$  (right panel of Figure 11).

#### 4.4.4. Object Detection Completeness

Another measure of effective imaging depth is the object detection completeness relative to deeper imaging data. We evaluated the detection completeness of DES DR1 through a comparison to public CFHTLenS data (Erben et al. 2013) using an overlap region centered on (R.A., decl.) =  $(34^\circ.5, -5^\circ.4)$  consisting of nine CFHTLenS fields in the W1 patch.<sup>88</sup> The CFHTLenS  $5\sigma$  magnitude limit for a  $2''$  aperture is  $g' = 25.58$ ,

$r' = 24.88$ ,  $i' = 24.54$ ,  $y' = 24.71$ , and  $z' = 23.46$ . To ensure full coverage in both surveys, we restricted the analysis to regions with CFHTLenS image mask value `MASK` = 0 and DES coverage fraction  $>99\%$  in the intersection of the *griz* bands (see Drlica-Wagner et al. 2018). The effective area of overlap in both surveys including masking is  $6.0 \text{ deg}^2$ .

Object matching is performed using a  $1''$  radius, and we require a robust flux measurement in the respective DES band ( $15 < \text{MAG\_AUTO} < 30$ ) that is roughly consistent with that of CFHTLenS (within 1 mag) for an object to count as “detected” in DES DR1.

The DES DR1 detection efficiency is defined as the fraction of CFHTLenS objects in a given flux interval that has a matched DES object passing the baseline quality cuts listed above, and it is expressed in the DES photometric system using converted flux measurement from CFHTLenS. The resulting detection efficiency curves are plotted in Figure 12. DES DR1 detection efficiencies are only plotted for the magnitude range brighter than the typical  $S/N = 5$  limiting magnitude of CFHTLenS. The 95% completeness magnitude threshold obtained from this test is  $g = 23.72$ ,  $r = 23.35$ ,  $i = 22.88$ , and  $z = 22.25$  (Table 1). CFHTLenS does not include comparable *Y*-band coverage.

Using the same baseline quality selection criteria of `FLAGS_[GRIZ] < 4` and `IMAFLAGS_ISO_[GRIZ] = 0`, we find that in each of the *griz* bands,  $\lesssim 1\%$  of DES objects with `MAG_AUTO` greater than 20 and less than the typical  $S/N = 5$  limiting magnitude of CFHTLenS lack a matched counterpart in CFHTLenS (Figure 12). This suggests that contamination from spurious objects in DES DR1 is also  $\lesssim 1\%$ . We expect that some fraction of unmatched DES objects are astrophysical transients or moving objects. Indeed, the spatial distribution of co-add objects with only one single-epoch detection across the *grizY* bands is concentrated along the ecliptic.

#### 4.5. Morphological Object Classification

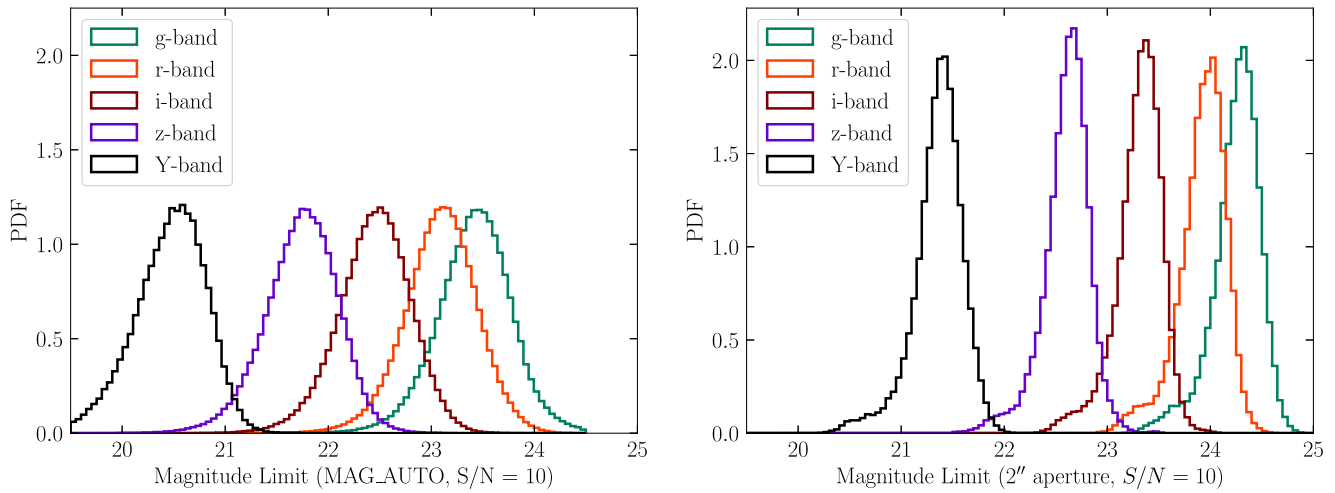
A basic selection on object size relative to the PSF can be used to separate samples of spatially extended galaxies from point-like stars and quasars. Accurate object classification becomes challenging for ground-based imaging surveys at faint magnitudes, and accordingly, optimal use of morphological, color, and temporal information is an active area of research (e.g., Fadelly et al. 2012; Małek et al. 2013; Bertin et al. 2015; Kim et al. 2015; Kim & Brunner 2017). Several object classification schemes have been applied to DES data for a variety of science cases (e.g., Chang et al. 2015; Reed et al. 2015; Soumagnac et al. 2015; Drlica-Wagner et al. 2018; Sevilla-Noarbe et al. 2018). The most common classification scheme makes use of the SExtractor `SPREAD_MODEL`, which compares the fit of a local PSF model to a slightly extended exponential disk model (Desai et al. 2012). Below we show an example using `SPREAD_MODEL` for object classification in a way that is suitable for both stellar and extragalactic science.

We define a new variable `EXTENDED_COADD` as the independent sum of several Boolean conditions:

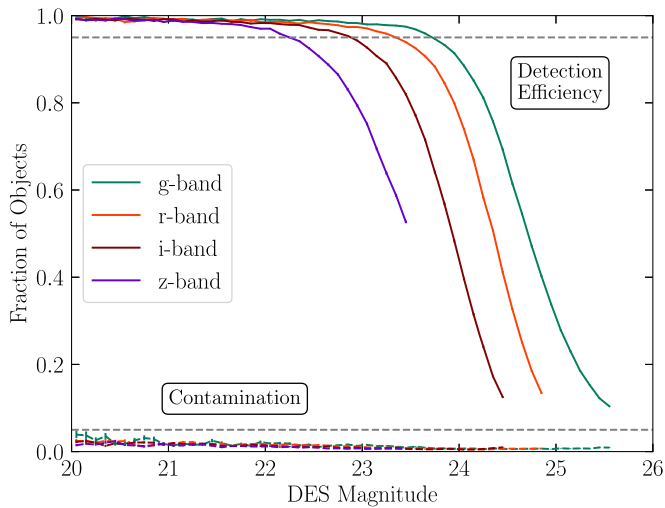
$$\begin{aligned} \text{EXTENDED\_COADD} &= ((\text{SPREAD\_MODEL\_I} + 3 \text{ SPREADERR\_MODEL\_I}) > 0.005) \\ &+ ((\text{SPREAD\_MODEL\_I} + \text{SPREADERR\_MODEL\_I}) > 0.003) \\ &+ ((\text{SPREAD\_MODEL\_I} - \text{SPREADERR\_MODEL\_I}) > 0.003). \end{aligned} \quad (2)$$

<sup>88</sup> CFHTLenS object catalogs and image masks available at <http://www.cfhtlenS.org/astronomers/data-store>.





**Figure 11.** Two estimates of the DES DR1 co-add catalog depth displayed as normalized histograms. Left: catalog depth estimated for MAG\_AUTO using catalog objects with  $S/N = 10$  ( $MAGERR\_AUTO = 0.10857$ ). Right: catalog depth for a  $2''$  aperture estimated from image properties using *mangle*. All magnitudes are given in the AB system.



**Figure 12.** DES DR1 detection efficiency and contamination relative to deeper imaging from CFHTLenS. Solid color curves represent the detection efficiency, while dashed color curves show the fraction of unmatched objects appearing only in DES. For visual reference, gray dashed lines indicate 5% and 95% of objects. DES magnitude is given in the AB system.

Note that `EXTENDED_COADD` is defined by a sequence of Boolean conditions that, when true, add a unit to the classifier. This classifier results in a value of 0 (high-confidence stars), 1 (likely stars), 2 (mostly galaxies), and 3 (high-confidence galaxies).

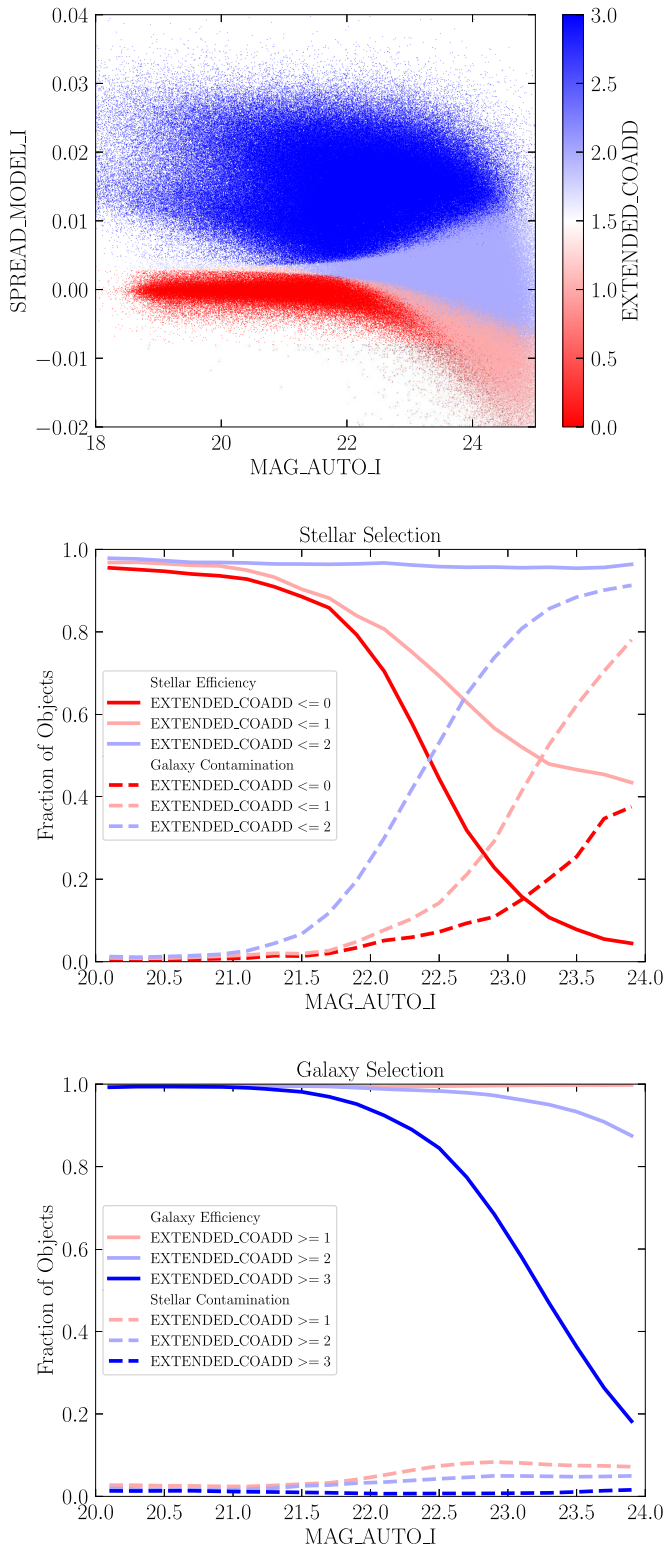
We evaluate the performance of the example classifier above using three regions in the main body of the DES footprint that overlap fields from HSC-SSP DR1 (Aihara et al. 2018b) with typical seeing in the *i*-band  $FWHM \lesssim 0''.7$ : SXDS (Ultra Deep layer), DEEP2\_3 (Deep layer), and portions of VVDS (Wide layer). The areal overlap between these HSC-SSP data sets and DES is  $\sim 18 \text{ deg}^2$ . The HSC-SSP data are of sufficient depth and image quality that a distinct stellar locus is clearly visible in the HSC concentration parameter  $\text{imag\_psf} - \text{icmodel\_mag}$  to an *i*-band magnitude of  $\sim 24.0$ . We choose empirically an interval of `EXTENDED_COADD` values to select stellar or galactic

samples with a balance of classification efficiency and purity appropriate for different science cases (Figure 13). Appendix C demonstrates how this classifier can be used in a number SQL query statement. Figure 14 shows density maps for stars and galaxies selected using `EXTENDED_COADD` equal to 0 and 3, respectively. For instance, one can define galaxy (`EXTENDED_COADD >= 2`) and stellar samples (`EXTENDED_COADD <= 1`) having  $\sim 310$  million and  $\sim 80$  million objects, respectively, following the standard object quality selection.

We recommend using quantities based on `SExtractor` `SPREAD_MODEL` for morphological classification in DR1. Although the `SExtractor` quantity `CLASS_STAR` has been commonly used in the past, we find that `SPREAD_MODEL`-based classifiers consistently outperform `CLASS_STAR`, as exemplified by the receiver operating characteristic (ROC) curve shown in Figure 15 and summarized in Table 3. The ROC curves are generated by performing a simple scan of threshold values for each of the `SExtractor` quantities and using the HSC-SSP classifications described above as a reference. Classifiers based on the weighted-average `SPREAD_MODEL` from single-epoch detections, `WAVG_SPREAD_MODEL`, are expected to be more robust for objects that are bright enough to be detected in single-epoch imaging (see Section 4.6). It is expected that classifiers using alternative bands and/or combinations of object measurements will be more appropriate for specific science cases.

#### 4.6. Known Issues

The PSF model has limited flexibility to accommodate discontinuities in the effective PSF that can occur in co-added images at boundaries in coverage between individual exposures. In these regions, the local PSF model can fail to accurately fit the point-like sources, and accordingly, both the co-add morphological classifications (i.e., `SPREAD_MODEL`, `CLASS_STAR`) and co-add PSF photometry are suspect. The photometry of extended sources is impacted to a lesser degree. Using the *i* band as an example, we identified such co-add PSF failures by searching for regions with anomalous co-add `SPREAD_MODEL_I` distributions and estimate that  $\lesssim 0.4\%$  of the footprint is substantially affected. Generally, more robust treatment (especially for point-like sources) is possible with



**Figure 13.** Stars and galaxies occupy distinct regions of spreadmodel-space at bright magnitudes but become more difficult to distinguish at faint magnitudes (top). DES DR1 object classification accuracy vs. HSC-SSP for both stellar (middle) and galaxy (bottom) samples. By using an interval of  $\text{EXTENDED\_COADD}$  values (Section 4.5), the balance of classification efficiency and purity can be adjusted as appropriate for specific science cases. DES magnitude is given in the AB system.

weighted-average quantities, at the cost of some loss of object detection completeness for the faintest sources (Figure 16). Due to the known issues in co-add PSF photometry, DES DR1 does

not include the co-add  $\text{MAG\_PSF}$  quantities. For studies of point-like sources, we recommend the use of  $\text{WAVG\_MAG\_PSF}$  (bright sources) or  $\text{MAG\_AUTO}$  (faint sources).

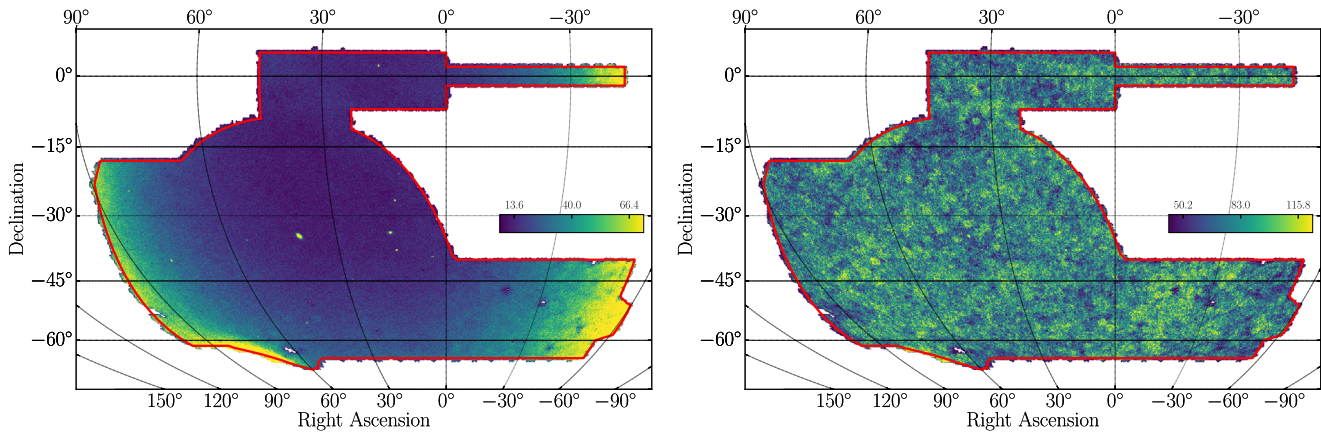
Among all the objects detected and cataloged,  $\sim 2.3\%$  have been flagged by  $\text{IMAFLAGS\_ISO}$  in at least one of the *grizY* bands, and  $\sim 0.1\%$  have artifacts in all five bands. As described in Section 4.3, it is recommended to use  $\text{IMAFLAGS\_ISO} = 0$  as a first filter of clean objects. Most of the objects with  $\text{IMAFLAGS\_ISO} = 1$  are saturated stars (Figure 17). A smaller fraction of flagged objects are missing imaging data in one or more of the bands, as shown in Figure 18, and usually have  $\text{NITER\_MODEL} = 0$ , which is set for objects that did not converge during the photometry measurement.

Scattered light from very bright stars can impact the photometry of nearby objects. Table 4 lists the coordinates and magnitudes of bright stars in the DES footprint. These stars generally cause ragged holes in the imaging coverage of DES DR1 owing to image-level blacklisting of scattered light artifacts (Figure 19). Scattered light from these stars extends beyond image- and catalog-level masking and can be observed at  $>1^\circ$  in the number counts of objects with extreme colors, i.e.,  $(g - r) > 4$  or  $(i - z) > 4$  (Drlica-Wagner et al. 2018). Additional care must be taken for analyses close to bright stars.

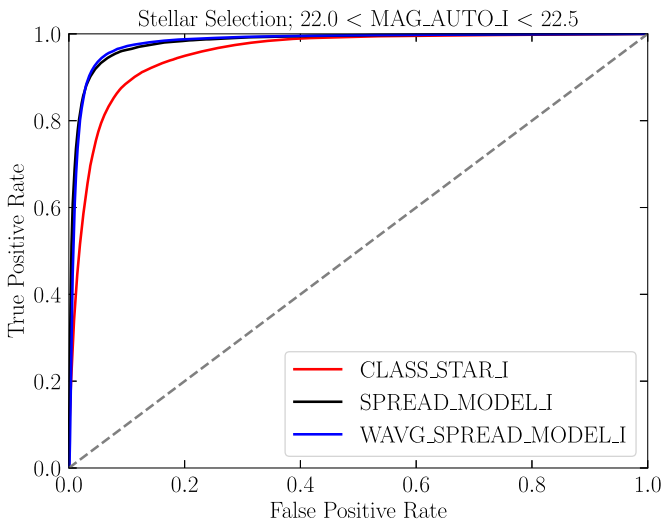
The DESDM processing pipeline is designed for extragalactic science at high Galactic latitudes. As such, it is not optimized to detect or measure sources in extremely crowded regions. Failures in source deblending are most noticeable in the cores of Galactic globular clusters, where source confusion and saturation reduce the catalog completeness appreciably. Table 5 lists five classical globular clusters within the DES DR1 footprint with integrated V-band magnitude brighter than 10 (Harris 1996, 2010 edition). The bottom panels of Figure 19 show two of these clusters, NGC 288 and NGC 1904, where saturation and source confusion can greatly impact source detection and photometric measurements. In addition, nearby bright galaxies (such as NGC 253, NGC 247, NGC 55, and IC 1613) are sometimes deblended into numerous individual objects, and some nearby edge-on spiral galaxies are partially masked.

The tabulated “DES DR1 standard bandpasses” (Figure 1, Section 5.4) included in this release were not the ones used to calculate the zero-points applied to the calibrated images and co-add source catalogs presented in DR1, but instead correspond to an earlier version of the system throughput referred to as the “Y3A1 standard bandpasses.” The latter system, which was the one available at the time of data processing, differs from the DES DR1 standard bandpasses in the treatment of the out-of-band system response. The DES DR1 standard bandpasses correct for a small inaccurate representation of *r*-band throughput in the Y3A1 standard bandpasses, which, due to an incorrect input calibration run, considered an unrealistically large light leakage relative to the in-band response ( $\sim 10^{-2}$ ) at wavelengths  $\sim 8000 \text{ \AA}$  and  $\sim 9200 \text{ \AA}$ . For co-add objects, the impact of setting the out-of-band response to zero in the DES DR1 standard bandpasses would lead to a photometry difference of  $\lesssim 2 \text{ mmag}$  (rms) in the *grizY* bands, which is below the level of statistical uncertainty in the co-add zero-points (Section 4.2).

A total of 59.5 of the 62 science CCDs in the DECam focal plane have been fully operational during the DR1 data collection period. CCD 61, which failed in 2012, was not processed for the DR1 data set. Similarly, CCD 2 was not processed between 2013 November and 2016 December



**Figure 14.** Left: stellar density map at HEALPix  $n_{\text{side}} = 1024$  resolution created with the EXTENDED\_COADD = 0 selection described in Section 4.5 (see also Appendix C). Discrete peaks in the stellar density correspond to globular clusters and dwarf galaxies in the Milky Way halo. Right: analogous galaxy density map created with the EXTENDED\_COADD = 3 selection. Color range units are number of objects per HEALPix  $n_{\text{side}} = 1024$  pixel.



**Figure 15.** ROC curve for a stellar selection in the magnitude range  $22.0 < \text{MAG\_AUTO\_I} < 22.5$  (AB system). The SPREAD\_MODEL outperforms CLASS\_STAR in classification accuracy of DES DR1 objects with respect to HSC-SSP. In this case, the SPREAD\_MODEL and WAVG\_SPREAD\_MODEL variants provide a very similar classification power, as denoted by the closely overlapping black and blue lines, respectively. The diagonal dashed line corresponds to the expectation from a random classifier.

(overlapping with observations included in this release), during which time it was not functional. Amplifier A of CCD 31 has an unpredictable, time-variable gain and is not included in this release. Amplifier B of CCD 31 functions normally and has been included. The rest of the science CCDs are performing within specifications and are usable for science. See Figure 20 for a layout of the DECam focal plane mosaic with the positions of affected CCDs marked.

## 5. Release Products

Here we detail the individual products included in DES DR1. The primary components of DES DR1 are derived from the union of 10,338 co-add tiles covering the DES footprint. The tile distribution for a portion of the SDSS Stripe 82 region is shown in the inset of Figure 2. To view all tiles and a HEALPix map ( $n_{\text{side}} = 32$ ) of 1753 pixels covering the entire DR1, visit <https://des.ncsa.illinois.edu/easyweb/footprint>.

### 5.1. Images

DES DR1 images can be grouped into two categories:

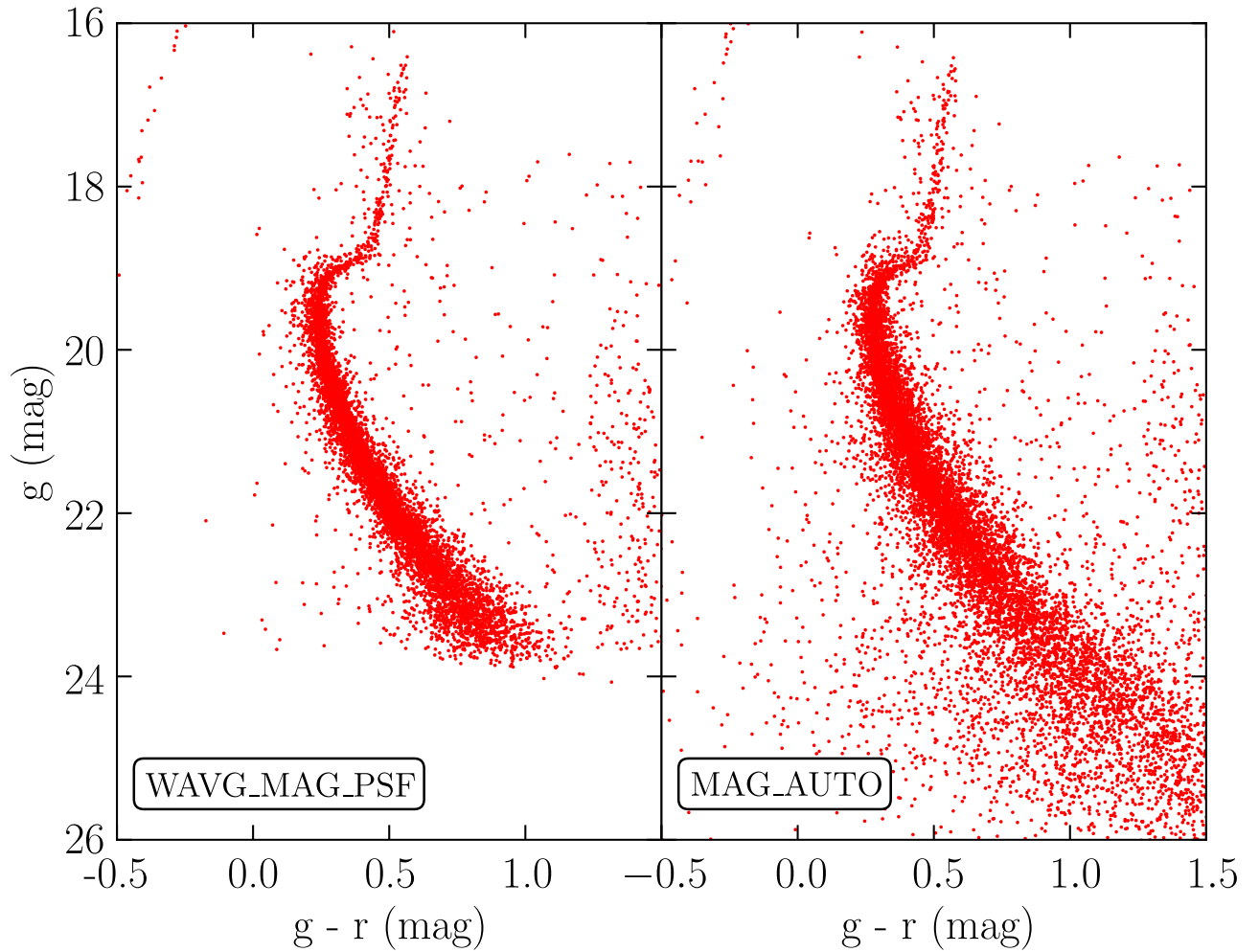
- Calibrated Single Exposures:** 38,850 exposures with photometric calibration, corresponding to 4,124,753 individual CCD images. The number of exposures per band is  $N_g = 7626$ ,  $N_r = 7470$ ,  $N_i = 7470$ ,  $N_z = 7753$ , and  $N_Y = 8531$ . Each raw exposure is  $\sim 0.5$  GB in size (compressed). These images can be accessed through NOAO Data Lab.<sup>89</sup>
- Co-add Images:** As a result of the multi-epoch pipeline described in Section 3, a total of 10,338 tiles of  $10k \times 10k$  pixels spanning  $0.7306$  deg on a side at a resolution of  $0.263$  arcsec pixel $^{-1}$  (see inset of Figure 2) were produced in each of the five bands. These images, along with the  $r + i + z$  combined detection image used, are publicly available, with a total of 62,028 images constituting  $\sim 11$  TB of data.

### 5.2. Catalogs

The co-add source extraction process detected and cataloged 399,263,026 distinct objects. Morphological object information includes object centroids, shape parameters, HEALPix indices, and processing flags. Several different photometric measurements and associated uncertainties are provided, including AUTO, PETRO, WAVG\_PSF, and assorted aperture magnitudes (Table 6). These measurements are distributed in three database tables: DR1\_MAIN, DR1\_MAGNITUDE, and DR1\_FLUX served from an Oracle database at NCSA. The DR1\_MAIN table contains all object information that is not a photometric measurement or uncertainty, augmented by MAG\_AUTO and WAVG\_MAG\_PSF (and associated uncertainties), and interstellar-extinction-corrected versions. The other two tables contain auxiliary magnitude and flux measurements (with associated uncertainties) in addition to extra information that is present in all three tables, such as coordinates, flags, and HEALPix indices. We note that these tables contain two sets of coordinates for the objects, namely, (RA, DEC) and (ALPHAWIN\_J2000, DELTAWIN\_J2000), which are computed in the same manner; the difference between them is that RA and

<sup>89</sup> <http://datalab.noao.edu/>





**Figure 16.** Color-magnitude diagram for a stellar sample selected within a  $15' \times 15'$  box centered on the M2 globular cluster (see Appendix C). The weighted-average PSF photometry from WAVG\_MAG\_PSF (left) yields a tighter locus but does not extend as deep as the MAG\_AUTO photometry (right). All magnitudes are given in the AB system.

**Table 3**

Stellar Classification Accuracy Quantified as the Area under the ROC Curve (AUC) in Three Flux Intervals, Using HSC-SSP as a Reference (see Figure 15)

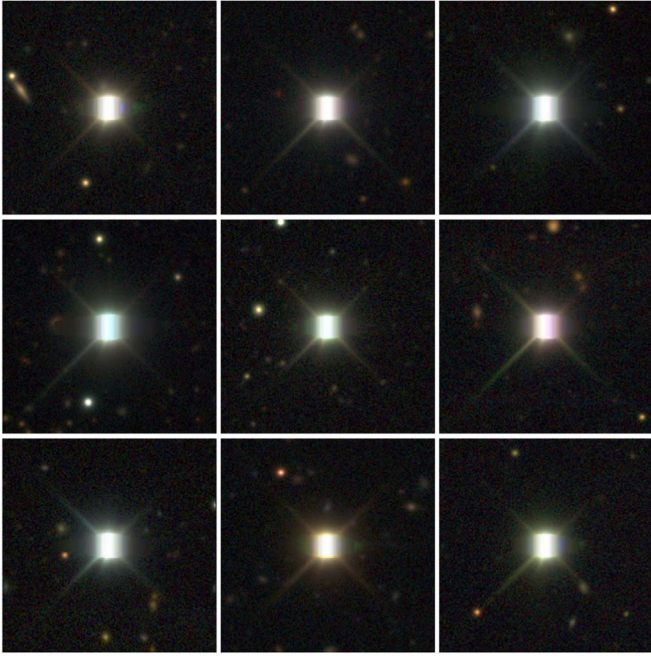
Quantity	WAVG_SPREAD_MODEL	SPREAD_MODEL	CLASS_STAR
$21.5 < \text{MAG\_AUTO\_I} < 22.0$	0.994	0.991	0.979
$22.0 < \text{MAG\_AUTO\_I} < 22.5$	0.981	0.981	0.954
$22.5 < \text{MAG\_AUTO\_I} < 23.0$	0.917	0.948	0.881

**Note.** In this case, the AUC statistic is the probability that the simple classifier will correctly rank a randomly chosen star higher than a randomly chosen galaxy. DES magnitude is given in the AB system.

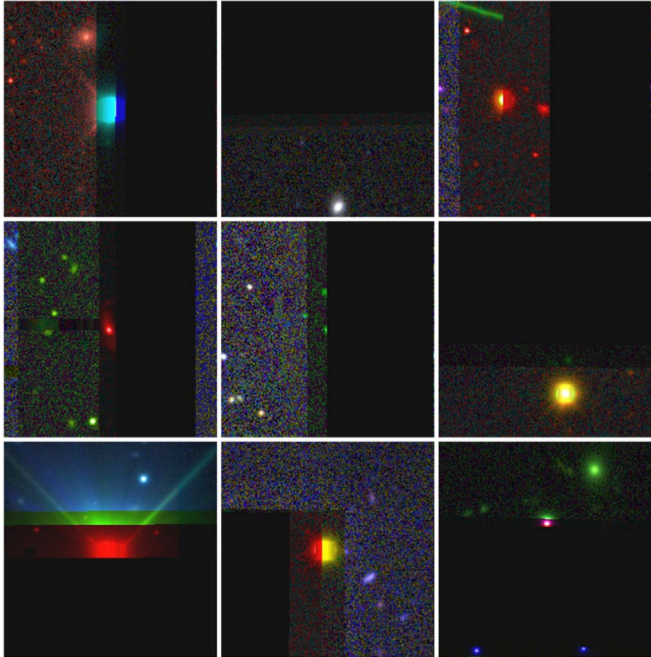
DEC are truncated to six decimals in order to provide a search indexing and table partitioning on these columns, while ALPHAWIN\_J2000 and DELTAWIN\_J2000 are double-precision quantities to be used when precise measurements are needed. All spatial-based queries should use RA and DEC in their condition statements. Additionally, the table DR1\_TILE\_INFO contains information about the processed tiles, such as sky location, geometry, number of objects, and file paths to access the associated images and object catalogs. For a complete description of these tables, we refer the reader to Appendix E.

### 5.3. Files

In order to provide a convenient way to download all the catalog data at once, and noting that the tile is the basic processing unit for the survey, we have created FITS file versions of the catalog tables grouped by co-add tile. This amounts to 31,014 total files (for the DR1\_MAIN, DR1\_MAGNITUDE, and DR1\_FLUX tables) with almost 2.5 TB of catalog data. Both the catalog and corresponding image file paths can be obtained from the DR1\_TILE\_INFO table (see Appendix C for an example) and can be accessed through the interfaces described in Section 6.



**Figure 17.** Composite *gri*  $1' \times 1'$  cutouts of saturated stars with `IMAFLAGS_ISO` = 1.

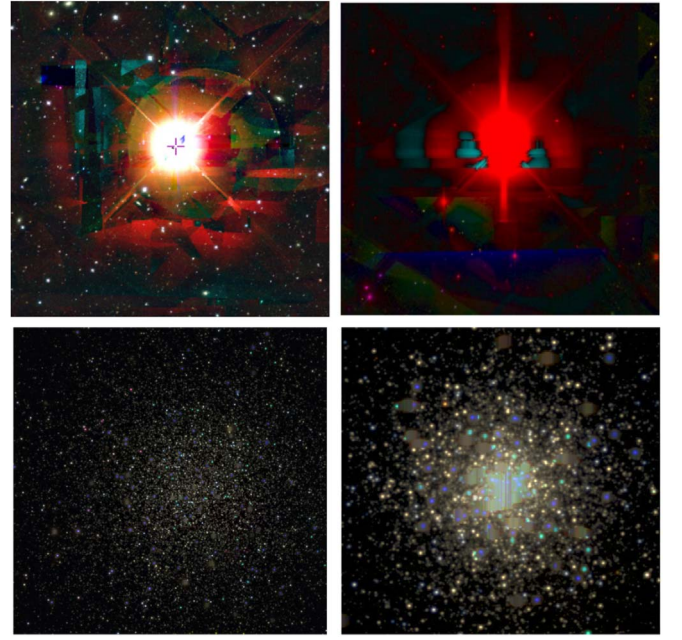


**Figure 18.** Composite *gri*  $1' \times 1'$  cutouts of objects with `IMAFLAG-S_ISO` = 1 and `NITER_MODEL` = 0. The majority of such objects, but not all, have missing imaging data.

#### 5.4. DES DR1 Standard Bandpasses

DES DR1 includes an updated characterization of the Blanco/DECam total system response (instrument and atmosphere) for the *grizY* bands (Figure 1).<sup>90</sup> The DES DR1 standard bandpasses are defined as the average CCD response across the focal plane as measured with the DECam system (Marshall et al. 2013), together with a standard atmospheric transmission computed with the

<sup>90</sup> <http://www.ctio.noao.edu/noao/content/DECam-filter-information>



**Figure 19.** Examples of very bright stars, *R* Dor ( $30' \times 30'$  cutout; top left) and  $\alpha$  Phe ( $14' \times 14'$  cutout; top right), and globular clusters, NGC 288 ( $8' \times 8'$  cutout; bottom left) and NGC 1904 ( $2.5' \times 2.5'$  cutout; bottom right), found within the DES DR1 footprint.

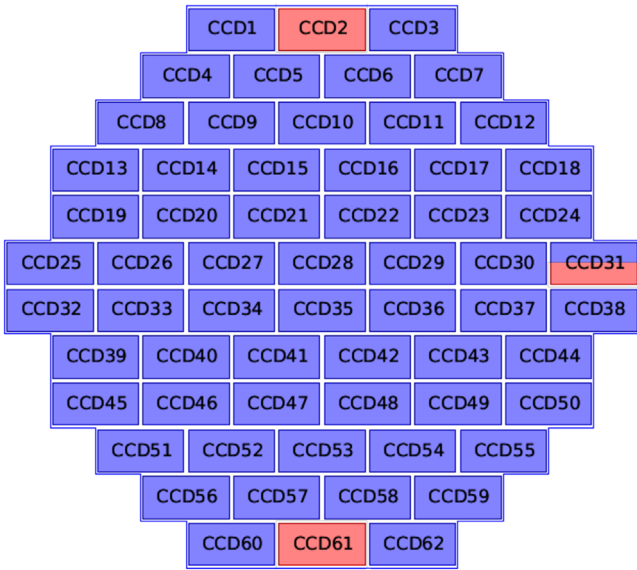
**Table 4**  
List of Very Bright Stars within the DES Footprint

Star	R.A. (deg)	Decl. (deg)	Apparent Magnitude (V mag)
$\alpha$ Col (Phact)	84.9121	-34.0741	2.65
$\alpha$ Phe (Ankaa)	6.5708	-42.3061	2.38
$\alpha$ Eri (Achernar)	24.4288	-57.2367	0.46
$\alpha$ Hya (Alphard)	29.6925	-61.5697	2.00
$\gamma$ Eri (Zaurak)	59.5075	-13.5086	2.91
<i>R</i> Dor	69.1900	-62.0775	5.40
$\alpha$ Car (Canopus)	95.9879	-52.6958	-0.74
$\alpha$ Pav (Peacock)	306.4121	-56.7350	1.94
$\alpha$ Gru (Alnair)	332.0583	-46.9611	1.74
$\beta$ Gru (Tiaki)	340.6671	-46.8847	2.15

**Table 5**  
Brightest Globular Clusters within DES DR1

Globular Cluster	R.A. (deg)	Decl. (deg)	Apparent Magnitude (mag)
NGC 288	13.2	-26.58	8.1
NGC 1261	48.075	-55.13	8.4
NGC 1851	78.525	-40.05	7.3
NGC 1904	81.045	-24.523	8.0
NGC 7089	323.375	-0.8167	6.5

MODTRAN IV code (Berk et al. 1999) using parameters typical of the environmental conditions encountered during DES observations (for details, see Burke et al. 2017). For example, the air mass adopted for the standard atmosphere, 1.2, is well matched to the median air mass of exposures entering the co-add, 1.22. The system response is defined in steps of  $5 \text{ \AA}$  from  $3800 \text{ \AA}$  to  $11000 \text{ \AA}$ . Out-of-band light leakage has been directly measured with DECam to be  $\lesssim 10^{-3}$  relative to the in-band



**Figure 20.** DECam focal plane CCD layout oriented with north at the top and east on the right. The rectangles represent the 62 science CCDs, each of which is divided into two halves oriented along the long direction and read by two amplifiers. CCDs 2 and 61 were inactive for most of the DES data included in DR1. Amplifier A of CCD 31 has time-variable gain and has not been processed for this release. These areas are marked in red.

**Table 6**  
Diameters for the Set of Aperture Magnitudes

Column Name	Diameter (pixels)	Diameter (arcsec)
MAG_APER_1	1.85	0.49
MAG_APER_2	3.70	0.97
MAG_APER_3	5.55	1.46
MAG_APER_4	7.41	1.95
MAG_APER_5	11.11	2.92
MAG_APER_6	14.81	3.90
MAG_APER_7	18.52	4.87
MAG_APER_8	22.22	5.84
MAG_APER_9	25.93	6.82
MAG_APER_10	29.63	7.79
MAG_APER_11	44.44	11.69
MAG_APER_12	66.67	17.53

response, and vendor measurements of witness samples suggest that the out-of-band leakage is typically at the  $10^{-5}$  to  $10^{-4}$  level. While detailed characterization of the out-of-band response is ongoing, the throughput of the DES DR1 standard bandpasses is defined as zero for out-of-band wavelengths (caveats are mentioned in Section 4.6).

### 5.5. Software

All software used in the DESDM pipelines described in Section 3 and in Morganson et al. (2018) can be accessed from the release page itself<sup>91</sup> or from the DES Github Organization.<sup>92</sup> Together with access to the software used to generate these products and the configuration described in Morganson et al. (2018), we provide the main ingredients to reprocess the data in a manner similar to that done by DES.

## 6. Data Access

Access to the DES DR1 data is provided through a collaborative partnership between NCSA,<sup>93</sup> LineA,<sup>94</sup> and NOAO.<sup>95</sup> From these institutions, a rich and complementary set of tools and interfaces were developed to access and interact with DES data in different ways that cover a broad set of use cases that enable scientific discovery. In this section we describe the main tools provided to access DES DR1.<sup>96</sup>

### 6.1. NCSA DES access

NCSA provides the primary set of basic web applications to access DES DR1 data. Developed at NCSA, DESaccess (<https://des.ncsa.illinois.edu/easyweb>) provides the user with an interface to submit asynchronous jobs to perform SQL queries against an Oracle DB that contains the DES DR1 catalogs and to generate cutouts from a given list of positions from the co-add images. It also contains information regarding the catalogs, an interactive footprint finder to locate positions and tiles, and means to access images and catalogs in a tile-based format. The main services can be summarized as follows:

1. SQL web client: We provide an SQL web client that allows the user to submit asynchronous query jobs against the Oracle 12 database that contains the DES DR1 tables. The submitted jobs enter into a queue, and results can be retrieved at later times in either `csv`, `FITS` (Wells et al. 1981), or `HDF5` (The HDF Group 1997) file format, supporting compression in some of the cases. Big jobs are divided into chunks of 1.5 GB to facilitate file transfer. This interface also provides means to check syntax and to evaluate synchronous jobs for a quick view. Results files are served from an HTTP server that allows file transfer to remote machines. The query used and the results persist for a limited period of time under a “My-Jobs” tab. The query interface is powered using `easyaccess` (Carrasco Kind et al. 2018),<sup>97</sup> an enhanced SQL command-line interpreter designed for astronomical surveys and developed for DES.
2. Cutout server: The cutout server allows the user to generate cutouts up to  $12'$  on a side centered on a given set of positions. The returned files include cutouts in all bands, a cutout in the detection image, a color TIFF image created with STIFF (Bertin 2012) by combining the `gri` bands, and a PNG image. The typical sizes for these files are 85 MB for the FITS images, 9 MB for the color TIF, and 16 MB for the PNG version, for the case of a  $12' \times 12'$  cutout. These cutout jobs also go into a queue, and results files can be retrieved later and served remotely. The header of the cutouts is a copy from the original header from the images with extra keys indicating the center of the cutout `RA_CUTOUT` and `DEC_CUTOUT`. Results are preserved for a limited period and can also be retrieved under a “My-Jobs” tab within the web service. No stitching is performed for objects near the edge of the tile. This feature might be added in the future.

<sup>93</sup> <http://www.ncsa.illinois.edu/>

<sup>94</sup> <http://www.linea.gov.br/>

<sup>95</sup> <https://www.noao.edu/>

<sup>96</sup> <https://des.ncsa.illinois.edu/releases/dr1/dr1-access>

<sup>97</sup> <https://github.com/mgckind/easyaccess>

<sup>91</sup> <https://des.ncsa.illinois.edu/releases/dr1/dr1-docs/processing>

<sup>92</sup> <https://github.com/DarkEnergySurvey>



3. **Footprint:** A lightweight interactive tool that displays the DES footprint and its tiles. This tool can be used to search for a position in the sky and return the corresponding tile information, including name, corner coordinates, and list of files for download. It also allows searches by `TILENAME` (the tile name identifier) when the name is available. This service also provides access to all the processed tiles, including associated images and catalogs, directly from the file server.

The `DESaccess` code<sup>98</sup> and the release page<sup>99</sup> are open sourced. The front end was developed using web components, HTML, JS, and Polymer,<sup>100</sup> which allows the reuse of already-existing elements. The back end was mainly developed using the Python Tornado web-framework.<sup>101</sup> The submission jobs are handled by Celery,<sup>102</sup> which is a distributed queue manager written in Python. All of these applications are containerized using Docker,<sup>103</sup> and all the node resourcing and scheduling, as well as all the deployment, are managed by Kubernetes,<sup>104</sup> which allows us to run, manage, and scale containerized applications in a robust and efficient manner.

## 6.2. *LIneA Science Server*

The images and catalogs generated by DESDM for DR1 can also be accessed by an interface developed by the Laboratório Interinstitucional de e-Astronomia (LIneA) that supports the participation of Brazilian scientists in DES. It has been designed to offer ways to examine both images and catalogs, compare these with the results of other surveys, and examine the results of queries to the database. The interface consists of the following three services:

1. **Sky/Image viewer:** The Sky/Image viewer combination integrates third-party tools to allow the user to visualize the entire sky map produced by DES (Aladin Lite<sup>105</sup> developed by CDS<sup>106</sup>) in the form of an HIPs color-coded image, as well as each individual tile using VisiOmatic (Bertin et al. 2015). The native functions, such as zoom, have been augmented with (1) an image layer that allows the display of other surveys; (2) a position locator; (3) the possibility of sharing a display with other users; (4) a map viewer that allows the display of HEALpix maps generated during the processing of the data (e.g., a map of the number of images available at each point in the sky); (5) different grids and polyines, including the original co-add tiles and the border of the DES footprint; and (6) access to the image of a specific tile, which can be examined using VisiOmatic.

The image viewer can be used to examine the tile as a whole and to inspect a specific position on the sky in more detail using the native functions of the tool that include snapshot, profile overlays, contrast settings, color mix, zoom, full-screen mode, and catalog overlay. The

interface also allows side-by-side comparison of the same sky region using different settings. Other useful functions are the ability to switch on/off markers, recenter the display to provide a visualization of the entire tile, crop part of the image, and download the fits images and catalog associated with the tile being displayed.

Finally, one can also overlay object catalogs, which are classified into three categories: (1) targets—list of positions or objects either uploaded or created using the Target viewer and User Query services described below; (2) object catalog—the DES DR1 object catalog produced by DESDM; and (3) external catalogs—a sample of catalogs available in Vizier. To facilitate the comparison between catalogs, the user can change the symbol, color, and size of each catalog it selects to display.

2. **Target Viewer:** This service enables the user to examine a list of uploaded positions of objects selected using the User Query service described below. The first page provides a summary of the available target lists, the ability to upload/delete lists, and the ability to mark favorite lists. Adding a list can be done by pasting a list of (R.A., decl.) coordinates. Once a list is selected, the image surrounding an object/position can be visualized by selecting an entry in the list and the corresponding position. The user can then select the columns to be shown, sort according to a given attribute, and comment, rank, and reject an entry. One can also apply a filter, and the filtered list can be downloaded (as `CSV` or `FITS` file) or saved for future use.
3. **User Query:** This service provides access to the database table storing the DES DR1 data from which SQL queries can be written, validated, and executed. The resulting table is displayed under “My Tables,” where it can be renamed, a few lines of its content listed, and deleted. Objects selected can be immediately viewed in the Target Viewer after the columns of the resulting table are properly associated with those recognized by the tool.

Given the suite of functionalities available in each tool, tutorials in the form of videos have been prepared to help introduce first-time users to the services. Information about the current limitations is available in the help associated with each tool.

## 6.3. *NOAO Data Lab*

The NOAO Data Lab (Fitzpatrick et al. 2016) is one of the access portals for DES DR1. The goal of the Data Lab is to enable efficient exploration and analysis of large data sets, including catalogs, with a particular focus on surveys using DECam and the NOAO Mosaic cameras. Among its features are a database for catalog data, accessible both from a Table Access Protocol (TAP<sup>107</sup>) service and from direct PostgreSQL queries, web-based, command-line and programmatic catalog and image query interfaces (both custom and via standard VO protocols); remote storage space for personal database and files; a JupyterHub-based notebook analysis environment; and a Simple Image Access (SIA) service. The Data Lab hosts the DES DR1 catalog tables using a PostgreSQL v9.6 database on the back end. The data are identical to those hosted by the DES

<sup>98</sup> <https://github.com/mgckind/desaccess>

<sup>99</sup> [https://github.com/mgckind/des\\_ncsa](https://github.com/mgckind/des_ncsa)

<sup>100</sup> <https://www.polymer-project.org/>

<sup>101</sup> <http://www.tornadoweb.org/en/stable/>

<sup>102</sup> <http://www.celeryproject.org/>

<sup>103</sup> <https://www.docker.com/>

<sup>104</sup> <https://kubernetes.io/>

<sup>105</sup> <http://aladin.u-strasbg.fr/AladinLite/>

<sup>106</sup> <http://cdsportal.u-strasbg.fr/>

<sup>107</sup> <http://ivoa.net/documents/TAP>

Collaboration through the NCSA portal, but with a few additions: First, the Data Lab database contains tables with cross-matches to other large catalogs (AllWISE, GALEX, HSC, and Simbad) and a table of neighboring objects within a 30 arcsec radius for all objects in DES. Second, the main table contains a few extra columns, such as ecliptic and Galactic coordinates, an HTM<sup>108</sup> (Hierarchical Triangular Mesh) index, two supplementary HEALPix indices in RING ( $n_{\text{side}} = 256$ ) and NESTED ( $n_{\text{side}} = 4096$ ) schemes, and precomputed colors. Finally, the data are clustered and indexed using the Q3C scheme (Koposov & Bartunov 2006), allowing Q3C functions to perform fast spatial queries on the tables.

### 6.3.1. Data Lab Services

1. Both anonymous and authenticated access to DES DR1 through Data Lab services. Anonymous users of the Data Lab can query the DES DR1 database and use the web-based tools. By creating and logging into an account through [datalab.noao.edu](http://datalab.noao.edu), authenticated users get access to a dedicated Jupyter notebook server with permanently stored notebooks and 1 TB of storage space for personal database tables and files.
2. Access to DES DR1 through TAP. The Data Lab exposes the DES DR1 catalog through a TAP service, which may be accessed through a web query form and schema browser. Alternately, users may query DES DR1 through TOPCAT (Taylor 2005) by pointing to the URL of the Data Lab TAP service ([https://datalab.noao.edu/query.php?name=tap\\_schema.schemas](https://datalab.noao.edu/query.php?name=tap_schema.schemas)) from within the application.
3. Python and command-line query clients. The Data Lab client package (<https://github.com/noao-datalab/datalab-client>) contains the multipurpose `datalab` command-line interface and the `queryClient` Python module. Both interfaces allow synchronous queries from a personal computer, for which control is suspended until a result is returned, using either ADQL (the native TAP interface query language) or the Postgres SQL syntax. The user may also run asynchronous ADQL queries, for which the query operation is given a job ID and run in the background, through the TAP service. The `queryClient` module is preinstalled on the Data Lab Jupyter notebook server.
4. An image cutout service. The Data Lab SIA service provides access to cutouts of the DES DR1 images. For a given position on the sky, the SIA service returns a table of metadata of all images that fall within the specified radius. The metadata include select header information for each image, along with a URL to retrieve a cutout of a specified size.
5. A JupyterHub notebook server and compute environment. This server provides access to common Python libraries, as well as all Data Lab Python modules, including the `authClient` authorization module, the `queryClient` query module, the `storeClient` virtual storage module, other interface modules, and multiple examples. The Jupyter notebook server provides a convenient way to run code close to the data.

More information on using these services is available on the Data Lab web page: <http://datalab.noao.edu>.

## 7. Summary and Future Releases

DES has provided a deep view of the south Galactic cap with precise *grizY* photometry that will ultimately reach  $\sim 24$ th magnitude in the *i* band over  $\sim 5000$  deg<sup>2</sup>. We have described here an overview of the survey, data acquisition, and processing pipelines and have given more details on the release products, the data validation, the known issues, and the data access services for the first major public release (DR1).

This release is composed of the reduced images and wide-field co-add source catalogs from the first 3 yr of full science operations, consisting of almost 39,000 single exposure images and close to 62,000 co-add images (including all bands and detection images) covering 10,338 tiles over the DES footprint, resulting in nearly 400 million distinct cataloged objects. Benchmark galaxy and stellar samples contain  $\sim 310$  million and  $\sim 80$  million objects, respectively, following a basic object quality selection.

The primary attributes of DES DR1 are summarized in Table 1, and the data products can be accessed from several complementary platforms hosted at NCSA, NOAO, and LIneA, available at <https://des.ncsa.illinois.edu/releases/dr1>. The overall high quality and homogeneity of the release will provide a rich legacy for the international astrophysics community (e.g., Dark Energy Survey Collaboration et al. 2016).

DES finishes its scheduled observations in early 2019, and we expect that the next major public DES data release (DR2) will be based on the products available after the survey is completed.

Funding for the DES Projects has been provided by the U.S. Department of Energy, the U.S. National Science Foundation, the Ministry of Science and Education of Spain, the Science and Technology Facilities Council of the United Kingdom, the Higher Education Funding Council for England, the National Center for Supercomputing Applications at the University of Illinois at Urbana-Champaign, the Kavli Institute of Cosmological Physics at the University of Chicago, the Center for Cosmology and Astro-Particle Physics at the Ohio State University, the Mitchell Institute for Fundamental Physics and Astronomy at Texas A&M University, Financiadora de Estudos e Projetos, Fundação Carlos Chagas Filho de Amparo à Pesquisa do Estado do Rio de Janeiro, Conselho Nacional de Desenvolvimento Científico e Tecnológico and the Ministério da Ciência, Tecnologia e Inovação, the Deutsche Forschungsgemeinschaft, and the Collaborating Institutions in the Dark Energy Survey.

The Collaborating Institutions are Argonne National Laboratory, the University of California at Santa Cruz, the University of Cambridge, Centro de Investigaciones Energéticas, Medioambientales y Tecnológicas-Madrid, the University of Chicago, University College London, the DES-Brazil Consortium, the University of Edinburgh, the Eidgenössische Technische Hochschule (ETH) Zürich, Fermi National Accelerator Laboratory, the University of Illinois at Urbana-Champaign, the Institut de Ciències de l'Espai (IEEC/CSIC), the Institut de Física d'Altes Energies, Lawrence Berkeley National Laboratory, the Ludwig-Maximilians Universität München and the

<sup>108</sup> <http://www.skyserver.org/htm>

associated Excellence Cluster Universe, the University of Michigan, the National Optical Astronomy Observatory, the University of Nottingham, The Ohio State University, the University of Pennsylvania, the University of Portsmouth, SLAC National Accelerator Laboratory, Stanford University, the University of Sussex, Texas A&M University, and the OzDES Membership Consortium.

Based in part on observations at the Cerro Tololo Inter-American Observatory, National Optical Astronomy Observatory, which is operated by the Association of Universities for Research in Astronomy (AURA) under a cooperative agreement with the National Science Foundation.

The DES data management system is supported by the National Science Foundation under grant nos. AST-1138766 and AST-1536171. The DES participants from Spanish institutions are partially supported by MINECO under grants AYA2015-71825, ESP2015-66861, FPA2015-68048, SEV-2016-0588, SEV-2016-0597, and MDM-2015-0509, some of which include ERDF funds from the European Union. IFAE is partially funded by the CERCA program of the Generalitat de Catalunya. Research leading to these results has received funding from the European Research Council under the European Union's Seventh Framework Program (FP7/2007-2013), including ERC grant agreements 240672, 291329, and 306478.

Members of LIneA would like to acknowledge the financial support of the special program INCT do e-Universo.

This work made use of the Illinois Campus Cluster, a computing resource that is operated by the Illinois Campus Cluster Program (ICCP) in conjunction with the National Center for Supercomputing Applications (NCSA) and is supported by funds from the University of Illinois at Urbana-Champaign.

This research is part of the Blue Waters sustained-petascale computing project, which is supported by the National Science Foundation (awards OCI-0725070 and ACI-1238993) and the state of Illinois. Blue Waters is a joint effort of the University of Illinois at Urbana-Champaign and its National Center for Supercomputing Applications.

We acknowledge support from the Australian Research Council Centre of Excellence for All-sky Astrophysics (CAASTRO), through project no. CE110001020, and the Brazilian Instituto Nacional de Ciência e Tecnologia (INCT) e-Universe (CNPq grant 465376/2014-2).

This manuscript has been authored by Fermi Research Alliance, LLC, under contract no. DE-AC02-07CH11359 with the U.S. Department of Energy, Office of Science, Office of High Energy Physics. The United States Government retains and the publisher, by accepting the article for publication, acknowledges that the United States Government retains a nonexclusive, paid-up, irrevocable, worldwide license to publish or reproduce the published form of this manuscript, or allow others to do so, for United States Government purposes.

*Facility:* Blanco (DECam).

*Software:* SExtractor (Bertin & Arnouts 1996), PSFEX (Bertin 2011), scamp (Bertin 2006), swarp (Bertin 2010), mangle (Hamilton & Tegmark 2004; Swanson et al. 2008), HEALPix (Górski et al. 2005),<sup>109</sup> astropy (Astropy Collaboration et al. 2013), matplotlib (Hunter 2007),

numpy (Van Der Walt et al. 2011), scipy (Jones et al. 2001), healpy,<sup>110</sup> fitsio,<sup>111</sup> ngmix (Sheldon 2014),<sup>112</sup> easy-access, skymap.

## Appendix A DES Terminology

1. Image: a single raw output file corresponding to 1 of the 62 science CCDs in the DECam focal plane.
2. Hex: a hexagonal field on the sky nominally covered by the 62 science CCDs of a single DECam pointing.
3. Exposure: a collection of 62 science CCD images corresponding to a single pointing of DECam.
4. Tiling: a collection of DECam pointings that covers the DES footprint with minimal gaps and overlaps in a single filter.
5. Tile: a sky area unit used by DESDM to parcel the DES footprint and organize the co-add outputs. Each tile is 0°.7306 on a side.
6. Single-epoch: relates to the collection and analysis of individual exposures for a single band prior to co-addition.
7. Co-add: the process of combining the data from multiple exposures over an area in order to increase depth.
8. Y3A2 Release: second annual internal release by DESDM to the DES Collaboration of data products obtained from the first three seasons of DES science operations and the Science Verification period. DR1 is based on Y3A2.

## Appendix B Photometric Transformations

We provide empirical photometric transformations between DES and other surveys that were used for the validation of DR1 data products.

### B.1. Gaia

A sample of stars taken from the deep SN fields with at least 25 observations in each of the  $g$ ,  $r$ , and  $i$  bands were matched to *Gaia* stars with  $G < 20$  mag. The *Gaia*  $G$ -band magnitudes predicted from from DES photometry are

$$G = r - 0.100 + 0.150(g - i) - 0.013(g - i)^2 - 0.035(g - i)^3, \quad (3)$$

valid for stars with  $0.3 < g - i < 3.0$ .

### B.2. CFHTLenS

As described in Section 4.4, we transformed photometry from the CFHTLenS survey to the DES system to report the detection efficiency of CFHTLenS objects as a function of magnitude in the DES system. The corresponding transformation equations, which were empirically derived from matched stars with high

<sup>109</sup> <http://healpix.sourceforge.net>

<sup>110</sup> <https://github.com/healpy/healpy>

<sup>111</sup> <https://github.com/esheldon/fitsio>

<sup>112</sup> <https://github.com/esheldon/ngmix>



measured S/N, are

$$\begin{aligned} g_{\text{DES}} &= g_{\text{CFHTLenS}} + 0.040(g - r)_{\text{CFHTLenS}} + 0.143 \\ r_{\text{DES}} &= r_{\text{CFHTLenS}} - 0.083(g - r)_{\text{CFHTLenS}} + 0.089 \\ i_{\text{DES}} &= i_{\text{CFHTLenS}} - 0.179(i - z)_{\text{CFHTLenS}} + 0.132 \\ z_{\text{DES}} &= z_{\text{CFHTLenS}} - 0.067(i - z)_{\text{CFHTLenS}} + 0.115. \end{aligned} \quad (4)$$

### Appendix C Example Queries

We provide several example SQL queries to the DR1 Oracle database tables. Note that these queries can be easily modified to ADQL language used by the TAP service at NOAO Data Labs.

1. Sample of objects: This query returns a sample of 0.0001% of objects from DR1.

```
SELECT ra, dec, mag_auto_g FROM
drl_main SAMPLE (0.0001);
```

also, one can select the first rows of a table with a command like

```
SELECT ra, dec, mag_auto_g FROM
drl_main WHERE ROWNUM <= 10.
```

2. Select stars from the M2 globular cluster: This query uses the EXTENDED\_COADD example morphological classifier to separate point-like stars from spatially extended galaxies (see Section 4.5). An interstellar reddening correction has been pre-applied to the columns marked with the `_dered` suffix (see Section 4.2). This query was used to generate Figure 16.

```
SELECT
  coadd_object_id,
  ra, dec, ebv_sfd98,
  mag_auto_g_dered,
  mag_auto_r_dered,
  wavg_mag_psf_g_dered,
  wavg_mag_psf_r_dered
FROM
  drl_main
WHERE
  ra BETWEEN 323.36 -125 AND
  323.36 +0.125
  AND dec BETWEEN -0.82 - 0.125
  AND -0.82 +0.125
  AND ((CASE WHEN spread_model_i
+ 3. * spreaderr_model_i > 0.005 THEN 1
ELSE 0 END) +
      (CASE WHEN spread_model_i +
1. * spreaderr_model_i > 0.003 THEN 1 ELSE
0 END) +
      (CASE WHEN spread_model_i-
1. * spreaderr_model_i > 0.003 THEN 1 ELSE
0 END) ) <= 1
  AND spread_model_i BETWEEN
-0.05 AND 0.05
  AND imaflags_iso_g = 0
  AND imaflags_iso_r = 0
  AND flags_g < 4
  AND flags_r < 4.
```

3. Create galaxy density map: Create a HEALPix (NEST schema, celestial coordinates) galaxy density map at resolution `nside = 1024` ( $\sim 3.4'$ ):

```
SELECT
```

```
  hpix_1024, COUNT(mag_auto_i),
AVG(mag_auto_i)
FROM
  drl_main
WHERE
  ((CASE WHEN spread_model_i + 3. *
spreaderr_model_i > 0.005 THEN 1 ELSE 0
END) +
    (CASE WHEN spread_model_i +
1. * spreaderr_model_i > 0.003 THEN 1 ELSE 0
END) +
    (CASE WHEN spread_model_i-1. *
spreaderr_model_i > 0.003 THEN 1 ELSE 0
END)) = 3
  AND spread_model_i BETWEEN
-0.05 AND 0.05
  AND imaflags_iso_i = 0
  AND flags_i < 4
  AND mag_auto_i < 23
GROUP BY
  hpix_1024.
```

4. Return URLs for the complete co-add object catalogs and *grizY* co-add images within a small patch of sky:

```
SELECT
  tilename,
  fits_drl_main,
  fits_image_g, fits_image_r, fit-
s_image_i, fits_image_z, fits_image_y
FROM
  drl_tile_info
WHERE
  ra_cent BETWEEN 30. AND 32.
  AND dec_cent BETWEEN -6.
  AND -4.
```

### Appendix D SExtractor Flags

Table 7 summarizes the standard warning flags provided by SExtractor, encoded in the `FLAGS` bitmask column for each band.

**Table 7**  
Summary of Bitmask Values and Warning Descriptions for the SExtractor `FLAGS` Column<sup>a</sup>

Bit	Description
1	The object has neighbors, bright and close enough to significantly bias the MAG AUTO photometry, or bad pixels (more than 10% of the integrated area affected)
2	The object was originally blended with another one
4	At least one pixel of the object is saturated (or very close to)
8	The object is truncated (too close to an image boundary)
16	Object's aperture data are incomplete or corrupted
32	Object's isophotal data are incomplete or corrupted
64	A memory overflow occurred during deblending
128	A memory overflow occurred during extraction

**Note.**

<sup>a</sup> Table data obtained from <https://www.astromatic.net/pubsvn/software/sextactor/trunk/doc/sextactor.pdf>.

## Appendix E

### Released Tables

The DR1 catalog data are mostly composed of four tables (Tables 8–11). DR1\_MAIN includes all the main quantities extracted from the co-add pipeline (Table 8) and important information about the objects. That table also includes MAG\_AUTO and WAVG\_MAG\_PSF, as well as the corresponding dereddened magnitudes.

DR1\_FLUX and DR1\_MAGNITUDE contain 15 different measurements of the fluxes and magnitudes (Tables 9 and 10, respectively) for each object. Additionally, these three tables share some commonly used columns to facilitate queries (by avoiding the need to join multiple tables). The fourth table, DR1\_TILE\_INFO (Table 11), contains information relevant to the processed tiles, from the tile geometry to the URLs of associated files.

**Table 8**  
DR1\_MAIN Table Description: 399,263,026 Rows; 213 Columns

Column Name	Description	Number of Columns
COADD_OBJECT_ID	Unique identifier for the co-added objects	1
TILENAME	Identifier of each one of the tiles on which the survey is gridded	1
RA	Right ascension, with quantized precision for indexing (ALPHAWIN_J2000 has full precision but not indexed) (deg)	1
ALPHAWIN_J2000	Right ascension for the object, J2000 in ICRS system (full precision but not indexed) (deg)	1
DEC	Declination, with quantized precision for indexing (DELTAWIN_J2000 has full precision but not indexed) (deg)	1
DELTAWIN_J2000	Declination for the object, J2000 in ICRS system (full precision but not indexed) (deg)	1
GALACTIC_L	Galactic longitude (deg)	1
GALACTIC_B	Galactic latitude (deg)	1
XWIN_IMAGE	X-centroid from windowed measurements on co-added image (pixels)	1
YWIN_IMAGE	Y-centroid from windowed measurements on co-added image (pixels)	1
XWIN_IMAGE_G,R,I,Z,Y	X-centroid from windowed measurements on co-added band image (pixels)	5
YWIN_IMAGE_G,R,I,Z,Y	Y-centroid from windowed measurements on co-added band images (pixels)	5
X2WIN_IMAGE_G,R,I,Z,Y	Second moment in $x$ -direction, from converged windowed measurements (pixel2)	5
ERRX2WIN_IMAGE_G,R,I,Z,Y	Uncertainty in second moment of $x$ -distribution centroid, from converged windowed measurements (pixel2)	5
Y2WIN_IMAGE_G,R,I,Z,Y	Second moment in $y$ -direction, from converged windowed measurements (pixel2)	5
ERRY2WIN_IMAGE_G,R,I,Z,Y	Uncertainty in second moment of $y$ -distribution centroid, from converged windowed measurements (pixel2)	5
XYWIN_IMAGE_G,R,I,Z,Y	Second moment in $xy$ -direction, from converged windowed measurements (pixel2)	5
ERRXYWIN_IMAGE_G,R,I,Z,Y	Uncertainty in second moment of $xy$ -distribution, from converged windowed measurements (pixel2)	5
HPIX_32,64,1024,4096,16384	Healpix identifier for its <code>nside</code> grid size, in a NESTED schema	5
NEPOCHS_G,R,I,Z,Y	Number of epochs the source is detected in single-epoch images	5
NITER_MODEL_G,R,I,Z,Y	Number of iterations in model-fitting photometric measurements	5
ISOAREA_IMAGE_G,R,I,Z,Y	Isophotal area of the co-added source (pixel2)	5
A_IMAGE	Major-axis size based on an isophotal model (pixels)	1
ERRA_IMAGE	Uncertainty in major-axis size, from isophotal model (pixels)	1
AWIN_IMAGE_G,R,I,Z,Y	Major-axis size, from second-order windowed moment measurements (pixels)	5
ERRAWIN_IMAGE_G,R,I,Z,Y	Uncertainty in major-axis size, from converged windowed measurement, assuming uncorrelated noise (pixels)	5
B_IMAGE	Minor-axis size based on an isophotal model (pixels)	1
ERRB_IMAGE	Uncertainty in minor-axis size, from isophotal model (pixels)	1
BWIN_IMAGE_G,R,I,Z,Y	Minor-axis size, from second-order windowed moment measurements (pixels)	5
ERRBWIN_IMAGE_G,R,I,Z,Y	Uncertainty in minor-axis size, from converged windowed measurement, assuming uncorrelated noise (pixels)	5
THETA_J2000	Position angle of source in J2000 coordinates, from nonwindowed measurement (deg)	1
ERRTHETA_IMAGE	Uncertainty in source position, from isophotal model (deg)	1
THETAWIN_IMAGE_G,R,I,Z,Y	Position angle of source, for converged windowed measurement grow from $x$ to $y$ (deg)	5
ERRTHETAWIN_IMAGE_G,R,I,Z,Y	Uncertainty in source position angle, from converged windowed measurement (deg)	5
FWHM_IMAGE_G,R,I,Z,Y	FWHM measured from the isophotal area, from elliptical growth curve, modeled in two dimensions (pixels)	5
FLUX_RADIUS_G,R,I,Z,Y	Half-light radius for the object, from elliptical growth curve, modeled in two dimensions (pixels)	5
KRON_RADIUS	Kron radius measured from detection image (pixels)	1
KRON_RADIUS_G,R,I,Z,Y	Kron radius measured from co-added image (pixels)	5
CLASS_STAR_G,R,I,Z,Y	Simple morphological extended source classifier. Values between 0 (galaxies) and 1 (stars). SPREAD_MODEL exhibits better performance for morphological classification.	5

**Table 8**  
(Continued)

Column Name	Description	Number of Columns
SPREAD_MODEL_G,R,I,Z,Y	Morphology based classifier based on comparison between a PSF versus exponential-PSF model.	5
SPREADERR_MODEL_G,R,I,Z,Y	Values closer to 0 correspond to stars, larger values correspond to galaxies Uncertainty in morphology based classifier based on comparison between PSF versus exponential-PSF model.	5
WAVG_SPREAD_MODEL_G,R,I,Z,Y	SPREAD MODEL using the weighted-average values from single-epoch detections	5
WAVG_SPREADERR_MODEL_G,R,I,Z,Y	Uncertainty in SPREAD MODEL using the weighted-average values from single-epoch detections	5
FLUX_AUTO_G,R,I,Z,Y	Aperture-flux measurement, elliptical model based on the Kron radius (ADU)	5
FLUXERR_AUTO_G,R,I,Z,Y	Uncertainty in aperture-flux measurement, elliptical model based on the Kron radius (ADU)	5
WAVG_FLUX_PSF_G,R,I,Z,Y	Weighted-average flux measurement of PSF fit single-epoch detections (ADU)	5
WAVG_FLUXERR_PSF_G,R,I,Z,Y	Uncertainty of weighted-average flux measurement of PSF fit single-epoch detections (ADU)	5
MAG_AUTO_G,R,I,Z,Y	Magnitude estimation, for an elliptical model based on the Kron radius (mag)	5
MAGERR_AUTO_G,R,I,Z,Y	Uncertainty in magnitude estimation, for an elliptical model based on the Kron radius (mag)	5
MAG_AUTO_G,R,I,Z,Y_DERED	Dereddened magnitude estimation (using SFD98), for an elliptical model based on the Kron radius (mag)	5
WAVG_MAG_PSF_G,R,I,Z,Y	Weighted-average magnitude, of PSF fit single-epoch detections (mag)	5
WAVG_MAGERR_PSF_G,R,I,Z,Y	Uncertainty of weighted-average magnitude, of PSF fit single-epoch detections (mag)	5
WAVG_MAG_PSF_G,R,I,Z,Y_DERED	Dereddened weighted-average magnitude (using SFD98) from PSF fit single-epoch detections (mag)	5
EBV_SFD98	$E(B-V)$ reddening coefficient from Schlegel, Finkbeiner & Davis, 1998 (mag)	1
BACKGROUND_G,R,I,Z,Y	Background level, by CCD-amplifier (mag)	5
FLAGS_G,R,I,Z,Y	Additive flag describing cautionary advice about source extraction process. Use less than 4 for well-behaved objects	5
IMAFLAGS_ISO_G,R,I,Z,Y	Flag identifying sources with missing/flagged pixels, considering all single-epoch images	5

**Table 9**  
DR1\_FLUX Table Description: 399,263,026 Rows, 179 Columns

Column Name	Description	Number of Columns
COADD_OBJECT_ID	Unique identifier for the co-added objects	1
TILENAME	Identifier of each one of the tiles on which the survey is gridded	1
RA	Right ascension, with quantized precision for indexing (ALPHAWIN_J2000 has full precision but not indexed) (deg)	1
ALPHAWIN_J2000	Right ascension for the object, J2000 in ICRS system (full precision but not indexed) (deg)	1
DEC	Declination, with quantized precision for indexing (DELTAWIN_J2000 has full precision but not indexed) (deg)	1
DELTAWIN_J2000	Declination for the object, J2000 in ICRS system (full precision but not indexed) (deg)	1
XWIN_IMAGE	X-centroid of source (from co-add detection image) (pixels)	1
YWIN_IMAGE	Y-centroid of source (from co-add detection image) (pixels)	1
HPIX_32,64,1024,4096,16384	Healpix identifier for its <code>nside</code> grid size, in a NESTED schema	5
FLUX_AUTO_G,R,I,Z,Y	Flux measurement, for an elliptical model based on the Kron radius (ADU)	5
FLUXERR_AUTO_G,R,I,Z,Y	Uncertainty in flux measurement, for an elliptical model based on the Kron radius (ADU)	5
FLUX_APER_1-12_G,R,I,Z,Y	Flux measurement for circular apertures (ADU)	60
FLUXERR_APER_1-12_G,R,I,Z,Y	Uncertainty in flux measurement for circular apertures (ADU)	60
FLUX_PETRO_G,R,I,Z,Y	Flux for a Petrosian radius (ADU)	5
FLUXERR_PETRO_G,R,I,Z,Y	Uncertainty in flux for a Petrosian radius (ADU)	5
WAVG_FLUX_PSF_G,R,I,Z,Y	Weighted-average flux, of PSF fit single-epoch detections (ADU)	5
WAVG_FLUXERR_PSF_G,R,I,Z,Y	Uncertainty of weighted-average flux, of PSF fit single-epoch detections (ADU)	5
PETRO_RADIUS_G,R,I,Z,Y	Petrosian radius (pixels)	5
EBV_SFD98	$E(B-V)$ reddening coefficient from Schlegel, Finkbeiner & Davis, 1998 (mag)	1
FLAGS_G,R,I,Z,Y	Additive flag describing cautionary advice about source extraction process. Use less than 4 for well-behaved objects	5
IMAFLAGS_ISO_G,R,I,Z,Y	Flag identifying sources with missing/flagged pixels, considering all single-epoch images	5



**Table 10**  
DR1\_MAGNITUDE Table Description: 399,263,026 Rows, 179 Columns

Column Name	Description	Number of Columns
COADD_OBJECT_ID	Unique identifier for the co-added objects	1
TILENAME	Identifier of each one of the tiles on which the survey is gridded	1
RA	Right ascension, with quantized precision for indexing (ALPHAWIN_J2000 has full precision but not indexed) (deg)	1
ALPHAWIN_J2000	Right ascension for the object, J2000 in ICRS system (full precision but not indexed) (deg)	1
DEC	Declination, with quantized precision for indexing (DELTAWIN_J2000 has full precision but not indexed) (deg)	1
DELTAWIN_J2000	Declination for the object, J2000 in ICRS system (full precision but not indexed) (deg)	1
XWIN_IMAGE	X-centroid from windowed measurements on co-added image (pixels)	1
YWIN_IMAGE	Y-centroid from windowed measurements on co-added image (pixels)	1
HPIX_32,64,1024,4096,16384	Healpix identifier for its <i>nside</i> grid size, in a NESTED schema	5
MAG_AUTO_G,R,I,Z,Y	Magnitude estimation, for an elliptical model based on the Kron radius (mag)	5
MAGERR_AUTO_G,R,I,Z,Y	Uncertainty in magnitude estimation, for an elliptical model based on the Kron radius (mag)	5
MAG_APER_1–12_G,R,I,Z,Y	Magnitude estimation for circular apertures (mag)	60
MAGERR_APER_1–12_G,R,I,Z,Y	Uncertainty in magnitude estimation for circular apertures (mag)	60
MAG_PETRO_G,R,I,Z,Y	Magnitude for a Petrosian radius (mag)	5
MAGERR_PETRO_G,R,I,Z,Y	Uncertainty in magnitude for a Petrosian radius (mag)	5
WAVG_MAG_PSF_G,R,I,Z,Y	Weighted-average magnitude, of PSF fit single-epoch detections (mag)	5
WAVG_MAGERR_PSF_G,R,I,Z,Y	Uncertainty of weighted-average magnitude, of PSF fit single-epoch detections (mag)	5
PETRO_RADIUS_G,R,I,Z,Y	Petrosian radius (pixels)	5
EBV_SFD98	$E(B-V)$ reddening coefficient from Schlegel, Finkbeiner & Davis, 1998 (mag)	1
FLAGS_G,R,I,Z,Y	Additive flag describing cautionary advice about source extraction process. Use less than 4 for well-behaved objects	5
IMAFLAGS_ISO_G,R,I,Z,Y	Flag identifying sources with missing/flagged pixels, considering all single-epoch images	5














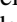


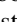


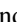























**Table 11**  
DR1\_TILE\_INFO Table Description: 10,338 Rows, 46 Columns

Column Name	Description	Number of Columns
TILENAME	Tilename identifier	1
RA_CENT	Central right ascension for tile (deg)	1
DEC_CENT	Central declination for tile (deg)	1
COUNT	Number of objects per tile	1
RAC1	Right ascension at corner 1 of tile (deg)	1
RAC2	Right ascension at corner 2 of tile (deg)	1
RAC3	Right ascension at corner 3 of tile (deg)	1
RAC4	Right ascension at corner 4 of tile (deg)	1
RACMAX	Maximum right ascension covered in tile (deg)	1
RACMIN	Minimum right ascension covered in tile (deg)	1
RA_SIZE	Extent of right ascension for tile (deg)	1
URAMAX	Maximum unique right ascension of objects measured from tile (deg)	1
URAMIN	Minimum unique right ascension of objects measured from tile (deg)	1
DECC1	Declination at corner 1 of tile (deg)	1
DECC2	Declination at corner 2 of tile (deg)	1
DECC3	Declination at corner 3 of tile (deg)	1
DECC4	Declination at corner 4 of tile (deg)	1
DECCMAX	Maximum declination covered in tile (deg)	1
DECCMIN	Minimum declination covered in tile (deg)	1
DEC_SIZE	Extent of declination for tile, in average is 0.7304 deg (deg)	1
UDECMAx	Maximum unique declination of objects measured from tile (deg)	1
UDECMIN	Minimum unique declination of objects measured from tile (deg)	1
CTYPE1	WCS projection used for axis 1. Value: RA—TAN	1
CTYPE2	WCS projection used for axis 2. Value: DEC—TAN	1
NAXIS1	WCS definition for number of pixels for axis 1	1
NAXIS2	WCS definition for number of pixels for axis 2	1
CRPIX1	WCS definition of central pixel for axis 1. Value: 5000.5	1
CRPIX2	WCS definition of central pixel for axis 2. Value: 5000.5	1
CRVAL1	WCS definition of central pixel value for axis 1	1
CRVAL2	WCS definition of central pixel value for axis 2	1

**Table 11**  
(Continued)

Column Name	Description	Number of Columns
CD1_1	WCS definition for pixel orientation. Value: $-0.0000730556$	1
CD1_2	WCS definition for pixel orientation. Value: 0	1
CD2_1	WCS definition for pixel orientation. Value: 0	1
CD2_2	WCS definition for pixel orientation. Value: $0.0000730556$	1
CROSSRA0	Flag tile boundary crosses RA = 0/24h boundary. Values: Y or N	1
PIXELSCALE	WCS definition of pixel scale. Values: 0.263 arcsec/pixel [arcsec/pixel]	1
TIFF_COLOR_IMAGE	Filename of the TIFF image for the tile, being tilename_r{reqnum}p{attnum}_irg.tiff	1
FITS_DR1_FLUX	Filename of the served FITS being tilename_dr1_flux.fits.fz	1
FITS_DR1_MAGNITUDE	Filename of the served FITS being tilename_dr1_magnitude.fits.fz	1
FITS_DR1_MAIN	Filename of the served FITS being tilename_dr1_main.fits.fz	1
FITS_IMAGE_DET	Filename of the served FITS being tilename_r{reqnum}p{attnum}_det.fits.fz	1
FITS_IMAGE_G,R,I,Z,Y	Filename of the served FITS, per band, being tilename_r{reqnum}p{attnum}_band.fits.fz	5

**ORCID iDs**

J. Annis  <https://orcid.org/0000-0002-0609-3987>  
S. Bocquet  <https://orcid.org/0000-0002-4900-805X>  
D. Brooks  <https://orcid.org/0000-0002-8458-5047>  
D. L. Burke  <https://orcid.org/0000-0003-1866-1950>  
M. Carrasco Kind  <https://orcid.org/0000-0002-4802-3194>  
F. J. Castander  <https://orcid.org/0000-0001-7316-4573>  
C. Conselice  <https://orcid.org/0000-0003-1949-7638>  
J. DeRose  <https://orcid.org/0000-0002-0728-0960>  
A. Drlica-Wagner  <https://orcid.org/0000-0001-8251-933X>  
J. García-Bellido  <https://orcid.org/0000-0002-9370-8360>  
D. W. Gerdes  <https://orcid.org/0000-0001-6942-2736>  
K. Glazebrook  <https://orcid.org/0000-0002-3254-9044>  
D. A. Goldstein  <https://orcid.org/0000-0003-3461-8661>  
D. Gruen  <https://orcid.org/0000-0003-3270-7644>  
R. A. Gruendl  <https://orcid.org/0000-0002-4588-6517>  
S. Hamilton  <https://orcid.org/0000-0002-6126-8487>  
D. Hollowood  <https://orcid.org/0000-0002-9369-4157>  
K. Kuehn  <https://orcid.org/0000-0003-0120-0808>  
P. Martini  <https://orcid.org/0000-0002-4279-4182>  
R. G. McMahon  <https://orcid.org/0000-0001-8447-8869>  
P. Melchior  <https://orcid.org/0000-0002-8873-5065>  
R. Miquel  <https://orcid.org/0000-0002-6610-4836>  
E. Morganson  <https://orcid.org/0000-0001-7180-109X>  
J. Mould  <https://orcid.org/0000-0003-3820-1740>  
B. Nord  <https://orcid.org/0000-0001-6706-8972>  
P. Nugent  <https://orcid.org/0000-0002-3389-0586>  
A. Palmese  <https://orcid.org/0000-0002-6011-0530>  
P. M. Ricker  <https://orcid.org/0000-0002-5294-0630>  
A. K. Romer  <https://orcid.org/0000-0002-9328-879X>  
A. Roodman  <https://orcid.org/0000-0001-5326-3486>  
N. Shipp  <https://orcid.org/0000-0003-2497-091X>  
M. Smith  <https://orcid.org/0000-0002-3321-1432>  
M. Soares-Santos  <https://orcid.org/0000-0001-6082-8529>  
F. Sobreira  <https://orcid.org/0000-0002-7822-0658>  
M. Sullivan  <https://orcid.org/0000-0001-9053-4820>  
G. Tarle  <https://orcid.org/0000-0003-1704-0781>  
A. K. Vivas  <https://orcid.org/0000-0003-4341-6172>  
A. R. Walker  <https://orcid.org/0000-0002-7123-8943>  
R. H. Wechsler  <https://orcid.org/0000-0003-2229-011X>  
B. Yanny  <https://orcid.org/0000-0002-9541-2678>  
S. Juneau  <https://orcid.org/0000-0002-0000-2394>  
D. Nidever  <https://orcid.org/0000-0002-1793-3689>  
K. Olsen  <https://orcid.org/0000-0002-7134-8296>

**References**

- Abazajian, K. N., Adelman-McCarthy, J. K., Agüeros, M. A., et al. 2009, *ApJS*, **182**, 543
- Aihara, H., Arimoto, N., Armstrong, R., et al. 2018a, *PASJ*, **70**, 4
- Aihara, H., Armstrong, R., Bickerton, S., et al. 2018b, *PASJ*, **70**, 8
- Astropy Collaboration, Robitaille, T. P., Tollerud, E. J., et al. 2013, *A&A*, **558**, A33
- Berk, A., Anderson, G. P., Bernstein, L. S., et al. 1999, *Proc. SPIE*, **3756**, 348
- Bernstein, G. M., Abbott, T. M. C., Desai, S., et al. 2017a, *PASP*, **129**, 114502
- Bernstein, G. M., Armstrong, R., Plazas, A. A., et al. 2017b, *PASP*, **129**, 074503
- Bertin, E. 2006, in ASP Conf. Ser. 351, *Astronomical Data Analysis Software and Systems XV*, ed. C. Gabriel et al. (San Francisco, CA: ASP), **112**
- Bertin, E. 2010, SWarp: Resampling and Co-adding FITS Images Together, *Astrophysics Source Code Library*, ascl:1010.068
- Bertin, E. 2011, in ASP Conf. Ser. 442, *Astronomical Data Analysis Software and Systems XX*, ed. I. N. Evans et al. (San Francisco, CA: ASP), **435**
- Bertin, E. 2012, in ASP Conf. Ser. 461, *Astronomical Data Analysis Software and Systems XXI*, ed. P. Ballester, D. Egret, & N. P. F. Lorente (San Francisco, CA: ASP), **263**
- Bertin, E., & Arnouts, S. 1996, *A&As*, **117**, 393
- Bertin, E., Mellier, Y., Radovich, M., et al. 2002, in ASP Conf. Ser. 281, *Astronomical Data Analysis Software and Systems XI*, ed. D. A. Bohlender, D. Durand, & T. H. Handley (San Francisco, CA: ASP), **228**
- Bertin, E., Pillay, R., & Marmo, C. 2015, *A&C*, **10**, 43
- Bohlin, R. C., Gordon, K. D., & Tremblay, P.-E. 2014, *PASP*, **126**, 711
- Burke, D., Rykoff, E. S., Allam, S., et al. 2017, arXiv:1706.01542
- Burke, D. L., Rykoff, E. S., Allam, S., et al. 2018, *AJ*, **155**, 41
- Calabretta, M. R., & Greisen, E. W. 2002, *A&A*, **395**, 1077
- Carlstrom, J. E., Ade, P. A. R., Aird, K. A., et al. 2011, *PASP*, **123**, 568
- Carrasco Kind, M., Drlica-Wagner, A., Koziol, A. M. G., & Petravick, D. 2018, arXiv:1810.02721
- Chang, C., Busha, M. T., Wechsler, R. H., et al. 2015, *ApJ*, **801**, 73
- Dark Energy Survey Collaboration, Abbott, T., Abdalla, F. B., et al. 2016, *MNRAS*, **460**, 1270
- de Jong, J. T. A., Verdoes Kleijn, G. A., Kuijken, K. H., & Valentijn, E. A. 2013, *ExA*, **35**, 25
- DES Collaboration 2005, arXiv:astro-ph/0510346
- DES Collaboration 2017, arXiv:1708.01530
- Desai, S., Armstrong, R., Mohr, J. J., et al. 2012, *ApJ*, **757**, 83
- Diehl, H. T., Neilsen, E., Gruendl, R., et al. 2014, *Proc. SPIE*, **9149**, 91490V
- Diehl, H. T., Neilsen, E., Gruendl, R., et al. 2016, *Proc. SPIE*, **9910**, 99101D
- Drlica-Wagner, A., Sevilla-Noarbe, I., Rykoff, E. S., et al. 2018, *ApJS*, **235**, 33
- Erben, T., Hildebrandt, H., Miller, L., et al. 2013, *MNRAS*, **433**, 2545
- Fadely, R., Hogg, D. W., & Willman, B. 2012, *ApJ*, **760**, 15
- Fitzpatrick, E. L. 1999, *PASP*, **111**, 63
- Fitzpatrick, M. 2010, in ASP Conf. Ser. 434, *Astronomical Data Analysis Software and Systems XIX*, ed. Y. Mizumoto, K.-I. Morita, & M. Ohishi (San Francisco, CA: ASP), **260**
- Fitzpatrick, M. J., Graham, M. J., Mighell, K. J., et al. 2016, *Proc. SPIE*, **9913**, 99130L
- Flaugher, B., Diehl, H. T., Honscheid, K., et al. 2015, *AJ*, **150**, 150
- Gaia Collaboration, Brown, A. G. A., Vallenari, A., et al. 2016, *A&A*, **595**, A2
- Górski, K. M., Hivon, E., Banday, A. J., et al. 2005, *ApJ*, **622**, 759

- Greisen, E. W., & Calabretta, M. R. 2002, *A&A*, **395**, 1061
- Gruen, D., Bernstein, G. M., Jarvis, M., et al. 2015, *JInst*, **10**, C05032
- Hamilton, A. J. S., & Tegmark, M. 2004, *MNRAS*, **349**, 115
- Harris, W. E. 1996, *AJ*, **112**, 1487
- Honscheid, K., DePoy, D. L. & for the DES Collaboration 2008, arXiv:0810.3600
- Honscheid, K., Elliott, A., Annis, J., et al. 2012, *Proc. SPIE*, **8451**, 845112
- Hunter, J. D. 2007, *CSE*, **9**, 90
- Ivezic, Z., Tyson, J. A., Abel, B., et al. 2008, arXiv:0805.2366
- Jones, E., Oliphant, T., Peterson, P., et al. 2001, SciPy: Open Source Scientific Tools for Python, <http://www.scipy.org/>
- Jordi, C., Gebran, M., Carrasco, J. M., et al. 2010, *A&A*, **523**, A48
- Kaiser, N., Burgett, W., Chambers, K., et al. 2010, *Proc. SPIE*, **7733**, 77330E
- Kessler, R., Marriner, J., Childress, M., et al. 2015, *AJ*, **150**, 172
- Kim, E. J., & Brunner, R. J. 2017, *MNRAS*, **464**, 4463
- Kim, E. J., Brunner, R. J., & Carrasco Kind, M. 2015, *MNRAS*, **453**, 507
- Koposov, S., & Bartunov, O. 2006, ASP Conf. Ser. 351, Astronomical Data Analysis Software and Systems XV, ed. C. Gabriel et al. (San Francisco, CA: ASP), 735
- Malek, K., Solarz, A., Pollo, A., et al. 2013, *A&A*, **557**, A16
- Marshall, J. L., Rheault, J.-P., DePoy, D. L., et al. 2013, arXiv:1302.5720
- Mohr, J. J., Armstrong, R., Bertin, E., et al. 2012, *Proc. SPIE*, **8451**, 84510D
- Morganson, E., Gruendl, R. A., Menanteau, F., et al. 2018, *PASP*, **130**, 074501
- Neilsen, E., & Annis, J. 2014, in ASP Conf. Ser. 485, Astronomical Data Analysis Software and Systems XXIII, ed. N. Manset & P. Forshay (San Francisco, CA: ASP), 77
- Oke, J. B. 1974, *ApJS*, **27**, 21
- Pogson, N. 1856, *MNRAS*, **17**, 12
- Reed, S. L., McMahon, R. G., Banerji, M., et al. 2015, *MNRAS*, **454**, 3952
- Rykoff, E. S., Rozo, E., & Keisler, R. 2015, arXiv:1509.00870
- Schlafly, E. F., & Finkbeiner, D. P. 2011, *ApJ*, **737**, 103
- Schlegel, D. J., Finkbeiner, D. P., & Davis, M. 1998, *ApJ*, **500**, 525
- Sevilla, I., Armstrong, R., Bertin, E., et al. 2011, arXiv:1109.6741
- Sevilla-Noarbe, I., Hoyle, B., Marchã, M. J., et al. 2018, arXiv:1805.02427
- Sheldon, E. S. 2014, *MNRAS*, **444**, L25
- Skrutskie, M. F., Cutri, R. M., Stiening, R., et al. 2006, *AJ*, **131**, 1163
- Soumagnac, M. T., Abdalla, F. B., Lahav, O., et al. 2015, *MNRAS*, **450**, 666
- Swanson, M. E. C., Tegmark, M., Hamilton, A. J. S., & Hill, J. C. 2008, *MNRAS*, **387**, 1391
- Taylor, M. B. 2005, in ASP Conf. Ser. 347, Astronomical Data Analysis Software and Systems XIV, ed. P. Shopbell, M. Britton, & R. Ebert (San Francisco, CA: ASP), 29
- The HDF Group 1997, NNNN, Hierarchical Data Format, version 5, <http://www.hdfgroup.org/HDF5/>
- Tyson, J. A. 2010, *Proc. SPIE*, **7733**, 773303
- Van Der Walt, S., Colbert, S. C., & Varoquaux, G. 2011, *CSE*, **13**, 22
- Wells, D. C., Greisen, E. W., & Harten, R. H. 1981, *A&AS*, **44**, 363
- York, D. G., Adelman, J., Anderson, J. E., Jr., et al. 2000, *AJ*, **120**, 1579